Article

Neuron

Orofacial Movements Involve Parallel Corticobulbar Projections from Motor Cortex to Trigeminal Premotor Nuclei

Highlights

- Focal activation of corticobulbar neurons in motor cortex evokes orofacial movements
- Corticobulbar neurons form orderly projections across multiple trigeminal subnuclei
- Trigeminal subnuclei, premotor for motor actions, project to multiple motor nuclei
- The cortico-trigemino-motoneuron network coordinates motor actions into a behavior

Authors

Nicole Mercer Lindsay, Per M. Knutsen, Adrian F. Lozada, Daniel Gibbs, Harvey J. Karten, David Kleinfeld

Correspondence

dk@physics.ucsd.edu

In Brief

How are orofacial behaviors formed from motor actions? Mercer Lindsay et al. delimit the control of forelimb, jaw, nose, and vibrissa movements. Neighboring neurons in motor cortex are shown to form projections that coordinate these movements via trigeminal premotor neurons.

Mercer Lindsay et al., 2019, Neuron *104*, 765–780
November 20, 2019
https://doi.org/10.1016/j.neuron.2019.08.032

CellPress

Neuron
Article

Orofacial Movements Involve Parallel Corticobulbar Projections from Motor Cortex to Trigeminal Premotor Nuclei

Nicole Mercer Lindsay,[1] Per M. Knutsen,[2] Adrian F. Lozada,[2] Daniel Gibbs,[3] Harvey J. Karten,[3] and David Kleinfeld[1,2,4,*]
[1]Section of Neurobiology, University of California, San Diego, La Jolla, CA 92093, USA
[2]Department of Physics, University of California, San Diego, La Jolla, CA 92093, USA
[3]Department of Neurosciences, University of California, San Diego, La Jolla, CA 92093, USA
[4]Lead Contact
*Correspondence: dk@physics.ucsd.edu
https://doi.org/10.1016/j.neuron.2019.08.032

SUMMARY

How do neurons in orofacial motor cortex (MCtx) orchestrate behaviors? We show that focal activation of MCtx corticobulbar neurons evokes behaviorally relevant concurrent movements of the forelimb, jaw, nose, and vibrissae. The projections from different locations in MCtx form gradients of boutons across premotor nuclei spinal trigeminal pars oralis (SpVO) and interpolaris rostralis (SpVIr). Furthermore, retrograde viral tracing from muscles that control orofacial actions shows that these premotor nuclei segregate their outputs. In the most dramatic case, both SpVO and SpVIr are premotor to forelimb and vibrissa muscles, while only SpVO is premotor to jaw muscles. Functional confirmation of the superimposed control by MCtx was obtained through selective optogenetic activation of corticobulbar neurons on the basis of their preferential projections to SpVO versus SpVIr. We conclude that neighboring projection neurons in orofacial MCtx form parallel pathways to distinct pools of trigeminal premotor neurons that coordinate motor actions into a behavior.

INTRODUCTION

The motor cortex (MCtx) orchestrates complex voluntary movements through its connections with an array of cortical and subcortical targets (Alloway et al., 2010; Graziano, 2016; Graziano et al., 2002; Hattox et al., 2002; Jeong et al., 2016; Mao et al., 2011; Oswald et al., 2013; Sreenivasan et al., 2015). In rodents, the bulk of the descending, corticobulbar projections from MCtx transmit signals through an array of collaterals that target many premotor nuclei in the brainstem (Alloway et al., 2010; Economo et al., 2018; Jeong et al., 2016; Kita and Kita, 2012). Yet despite these broad patterns of downstream connectivity, activation of neurons in MCtx can evoke clearly defined movements (Harrison et al., 2012; Hira et al., 2015). These past data suggest the existence of specific patterns of connectivity from corticobulbar to premotor neurons.

Like the case of neurons in MCtx, individual premotor neurons send broad collateral projections to other premotor, brainstem, and thalamic structures (Bellavance et al., 2017; Stanek et al., 2014; Yoshida et al., 1994). Furthermore, neighboring neurons in a premotor nucleus can broadly target multiple motor nuclei (Amri et al., 1990; Cunningham and Sawchenko, 2000; Dong et al., 2011; Fay and Norgren, 1997a, 1997b, 1997c; Li et al., 1995; Pinganaud et al., 1999; Takatoh et al., 2013), with some evidence that individual premotor neurons can target pairs of motor nuclei to potentially enact concurrent movements (Amri et al., 1990; Dong et al., 2011; Li et al., 1993; Stanek et al., 2014; Yoshida et al., 1994).

Here we investigate the nature of connectivity from corticobulbar to premotor neurons for orofacial pathways. Of particular interest are the inputs to secondary sensory neurons in the trigeminal complex that originate from MCtx (Jeong et al., 2016; Stanek et al., 2014; Takatoh et al., 2013; Yoshida et al., 1994). These sensory neurons are, in fact, also premotor neurons that are uniquely positioned to receive both unprocessed sensory information and high-level motor commands (Jacquin and Rhoades, 1990; Jacquin et al., 1986; Matthews et al., 2015; McElvain et al., 2018). Classic tracing, along with modern monosynaptic rabies-EnvA tracing, show that the oralis (SpVO) and rostral interpolaris (SpVIr) subnuclei of the spinal trigeminal nucleus project to motoneurons for the vibrissae (Erzurumlu and Killackey, 1979; Nguyen and Kleinfeld, 2005; Pinganaud et al., 1999; Takatoh et al., 2013), jaw (Li et al., 1995; Olsson and Westberg, 1991; Stanek et al., 2014; Westberg et al., 1998; Yoshida et al., 1994), tongue (Borke et al., 1983; Pinganaud et al., 1999; Stanek et al., 2014), eyelid (Gonzalez-Joekes and Schreurs, 2012; Hiraoka and Shimamura, 1977; May et al., 2012; van Ham and Yeo, 1996), nose (Kurnikova et al., 2019), and forelimb (Esposito et al., 2014). The results of these prior studies motivate the present study to delimit the involvement of SpVO and SpVIr in coordinating movements of the forelimbs, jaw, nose, and vibrissae.

The coordination of multiple motor actions into a clearly defined movement may use downstream premotor nuclei through labeled line or diverging projections. To discriminate among these possibilities, we ask, (1) What orofacial movements

are elicited by stimulating layer 5 pyramidal neurons in discrete locations of orofacial MCtx? (2) What then is the distribution of projections from orofacial MCtx to pools of premotor neurons in SpVO, SpVIr, and other trigeminal nuclei? Furthermore, how do these pools map onto muscles for different orofacial motor actions? (3) Does activation of SpVO- versus SpVIr-projecting neurons in MCtx evoke motor actions from a single orofacial appendage, consistent with signaling along a muscle-selective pathway that is used in different motor actions, or does this cortical activation coordinate multiple appendages in an action, consistent with an action-selective pathway? (4) Last, does the distinction between SpVO- and SpVIr-projecting activation show parallel signaling from MCtx through different pools of premotor neurons to enact different motor actions? We address these questions in awake, head-fixed mice using optogenetic-driven stimulation of genetically or virally labeled neurons coupled with electromyographic and videographic recording, along with anatomical tract tracing.

Background

The mammalian MCtx is defined by three types of maps: a cytoarchitectural map (Brecht et al., 2004; Brodmann and Gary, 2006; Donoghue and Wise, 1982), a muscle twitch map (Ferezou et al., 2007; Fritsch and Hitzig, 2009; Tennant et al., 2011), and a map of coherent movements (Graziano and Aflalo, 2007; Graziano et al., 2002; Hira et al., 2015). One of the first described features of the MCtx was that it was agranular, that is, lacking an identifiable layer 4 (Brodmann and Gary, 2006; Donoghue and Wise, 1982). In rodents, the cytoarchitecture map of MCtx is composed of two distinct regions, the agranular medial (AG_m) and agranular lateral (AG_l) areas (Donoghue and Wise, 1982; Tennant et al., 2011). AG_m cortex has a dense layer 2 with a pale layer 3. In contrast, layers 2 and 3 in AG_l cortex are largely indistinguishable (Donoghue and Wise, 1982; Tennant et al., 2011).

The muscle twitch map is a result of lowering the amplitude of electrical pulses applied to MCtx until only a dominant MCtx to muscle path dominates. Twitches of single muscles in the jaw, neck, and vibrissa are evoked in more rostral aspects, while those of the body and trunk are evoked in caudal aspects (Ferezou et al., 2007; Hollis et al., 2016; Tennant et al., 2011).

Although brief pulses of electrical stimulation can evoke muscle twitches, excitatory neurons in MCtx tend to be active throughout a movement (Churchland et al., 2012; Georgopoulos et al., 1986; Graziano et al., 2002; Peters et al., 2014). When electrical- or channelrhodopsin-based stimulations mimic these longer durations of activity in primates (Graziano and Aflalo, 2007; Graziano et al., 2002; Overduin et al., 2012) and rodents (Bonazzi et al., 2013; Harrison et al., 2012; Hira et al., 2015), complete motor acts are observed.

Although the muscle twitch map is a consequence of the minimum electrical stimulus required to evoke a twitch, at normal activity levels in behaving animals the representative region for a muscle would be larger and overlap with other muscles. Thus, the movement map is likely an expression of overlap of the many muscles required for movements. The synergy of muscle twitch and movement maps has begun to be elucidated by electrophysiological recordings of MCtx neurons (Kakei et al., 1999) and electromyographic recordings during intracranial microstimulation (Kakei et al., 1999; Overduin et al., 2012). These past results motivate the additional need to determine the relation of maps in MCtx with those in premotor subnuclei SpVO and SpVIr.

RESULTS

Orofacial Motor Cortex Muscle Mapping

Inspired by past work with primates (Graziano and Aflalo, 2007; Graziano et al., 2002), we first mapped behaviorally relevant orofacial movements evoked from MCtx. To characterize many orofacial appendages, we recorded the electromyograms (EMGs) of the biceps brachii, digastric, intrinsic vibrissa, masseter, quadriceps, and splenius capitis muscles, and we videographed concurrent motion of the forelimb, jaw, nose, and vibrissae during optical stimulation of MCtx in Thy1-ChR2 mice (Figures 1A–1D and 2A–2C; laser spot diameter 35 μm).

We modulated the incident laser power, while recording EMGs, at 2 of the intended 15 stimulation sites (Figure 1C, jaw and vibrissa MCtx stimulation sites outlined in green and purple, respectively) to determine the optimal power for mapping. Activation of motion either saturated or peaked at a power of 3.0 mW (Figure 1E). The final power was chosen to be below this value (i.e., 2.4 mW) (Figure 1E, arrows). As a means to map motor actions from many locations in orofacial MCtx (Figure 1C), we chose a 1 s, 30 Hz stimulus train (Figure 1D).

Composite maps of evoked amplitude were made for each muscle EMG and for nose and jaw movements across all stimulation sites. Significant activation or suppression of all EMG channels was found at all locations (five mice; $p < 0.001$, Kolmogorov-Smirnov [K-S] test). Some muscles, like the digastric and splenius capitis, exhibited "hotspots" of stronger activation from specific regions of MCtx, with smaller, yet still significant modulation from other stimulation locations (Figure 1F). The broad, low-level activation of all muscles is consistent with control of posture by MCtx, in addition to coordination of specific motor actions (Amundsen Huffmaster et al., 2017; Mimica et al., 2018; Overduin et al., 2012).

Examination of the composite maps for the jaw and neck muscles and jaw and nose movement show a division between the medial and lateral aspects of orofacial MCtx. The medial division has strong activation of the nose and splenius capitis muscles, while the lateral shows activation of the digastric and masseter muscles (Figure 1C, inset). This division likely reflects a predominant, albeit incomplete, segregation of exploratory movements to medial orofacial MCtx and feeding movements to lateral orofacial MCtx.

The biceps brachii, intrinsic vibrissa, and quadriceps muscles transcended the division of exploratory versus feeding areas (Figure 1F). We found that many stimulus sites evoked moderate activation of the intrinsic vibrissa muscle (Figure 1F), which is responsible for protraction of the vibrissae. Surprisingly, this muscle was strongly activated along the lateral part of orofacial MCtx (Figure 1F), a location that was not identified in mapping experiments performed with the animal under anesthesia (Ferezou et al., 2007; Haiss and Schwarz, 2005; Tennant et al., 2011; Kleinfeld et al., 2002). Consistent with previous work (Ferezou et al., 2007), we found only one stimulus location that evoked

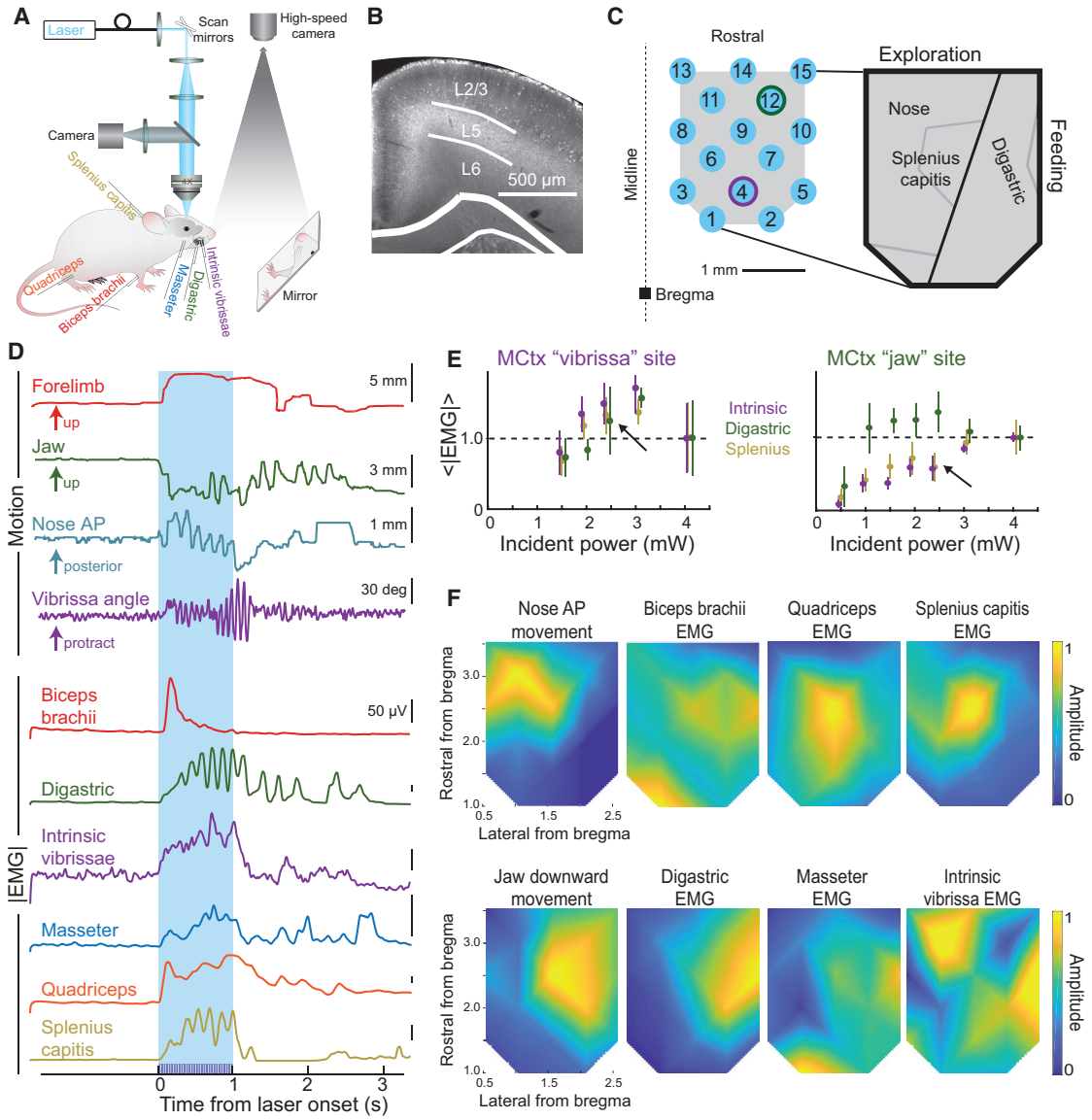

Figure 1. Orofacial Motor Cortex Map of Induced Muscle Activity, as Inferred from Movement and EMGs

(A) Schematic of laser activation of Thy1-ChR2-YFP mice with EMG recordings and high-speed videographs from above for the vibrissa and nose movements and using a mirror to reflect the forelimb and jaw movements up to the camera.

(B) Coronal section of Thy1-ChR2 mouse through MCtx with dense YFP labeling in layer 5.

(C) Schematic of positions targeted by a blue laser in MCtx for trials of 1 s of blue light. Jaw and vibrissa MCtx stimulus locations for (E) are identified by a green and purple outline of the laser spot, respectively. The expanded view is a summary of our observation that MCtx nominally partitions into a medial-exploratory region and a lateral-feeding division.

(D) Single trial examples of forelimb, jaw, nose, and vibrissa movements and biceps brachii, digastric, intrinsic vibrissa, masseter, quadriceps, and splenius capitis EMG envelopes. The blue box indicates the time the light train is ongoing. Examples are from a variety of stimulus locations, as labeled.

(E) Amplitude and standard deviation of the rectified EMG for the digastric, intrinsic vibrissa, and splenius capitis muscles from classic vibrissa MCtx (AP + 1.5 mm, ML 1.5 mm; purple outline in Figure 2C) compared with jaw MCtx (AP + 3 mm, ML 2 mm; green outline in Figure 2C) at different light intensities.

(F) Composite amplitude maps (five mice across a total of 15 days, interpolated between light points) for the biceps brachii, digastric, intrinsic vibrissa, quadriceps, and splenius capitis EMG envelope recordings and anterior-posterior nose and up-down jaw movements.

retraction of the vibrissa (Figures S1A and S1B). This site directly overlaps with large-amplitude activation of the splenius capitis neck muscle (Figure 1F), a muscle most strongly active during deep (90°–130°) head turns (Richmond et al., 1992; Roucoux et al., 1989). Furthermore, this location is in close proximity to the location where head turning movements have been evoked in freely moving mice (Barthas and Kwan, 2017). The combination of vibrissa retraction and large-amplitude activation of the

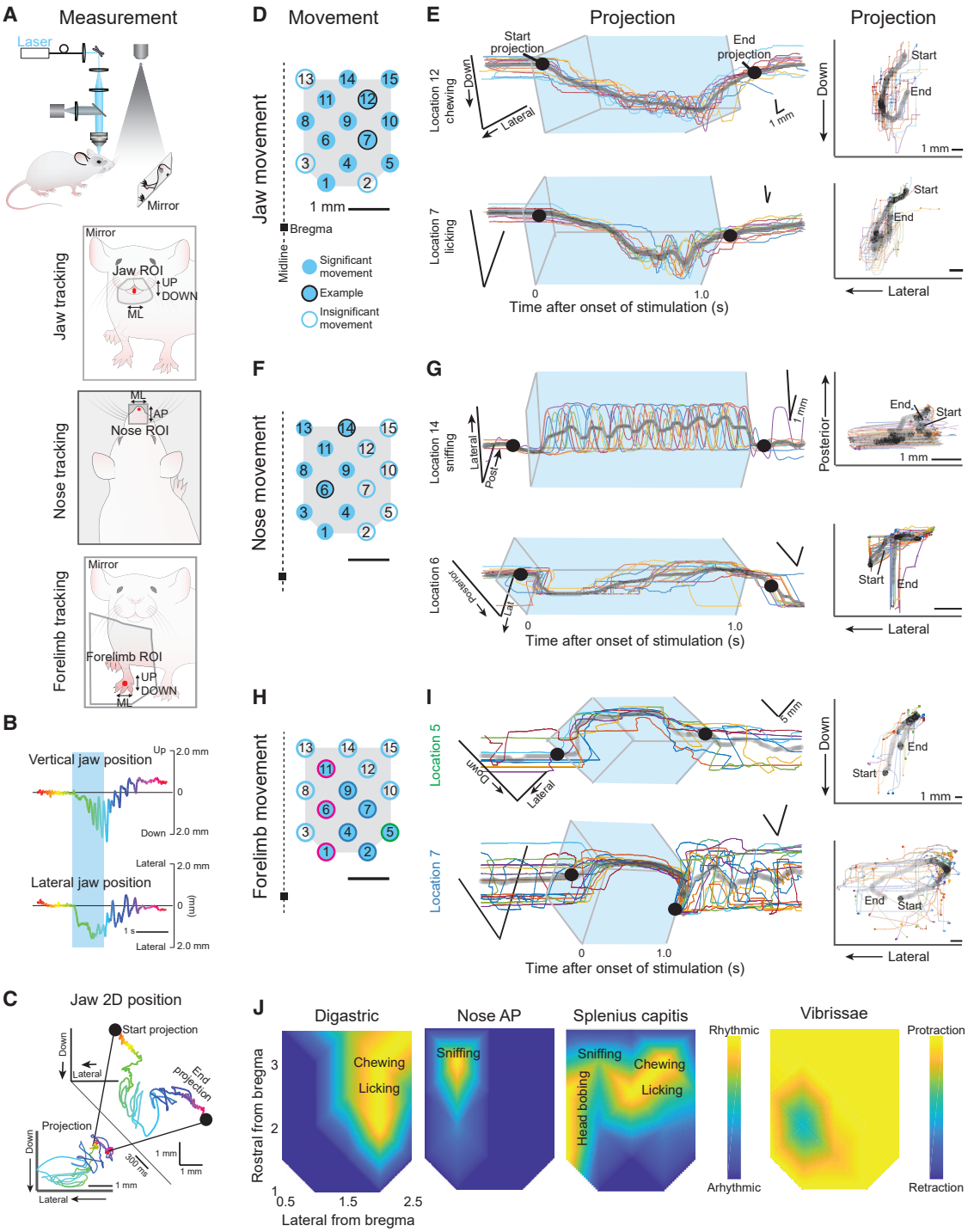

Figure 2. Mapping Orofacial Motor Cortex-Evoked Forelimb, Jaw, and Nose Movements, as Inferred from Videography

(A) Schematic of the videographic recording set up with the mirror image shown for tracking the jaw (left) and forelimb (right) and for the videography from above as done for the nose (middle).

(B) Single trial example of vertical (top) and lateral (bottom) jaw position.

(C) Conversion of single dimension positions in (B) to two-dimensional projection. Black dots illustrate the start and end of the projection (inset) that shows the movement path as observed looking on directly in the dimension of the mirror (forelimb and jaw) or from above (nose).

(D) Motor cortex stimulation points as seen in Figure 1C. Filled blue circles indicate locations where visible jaw movements were observed; black outlined circles indicate location from which jaw tracking examples are shown in (E). Movements were similarly observed in all five mice.

(legend continued on next page)

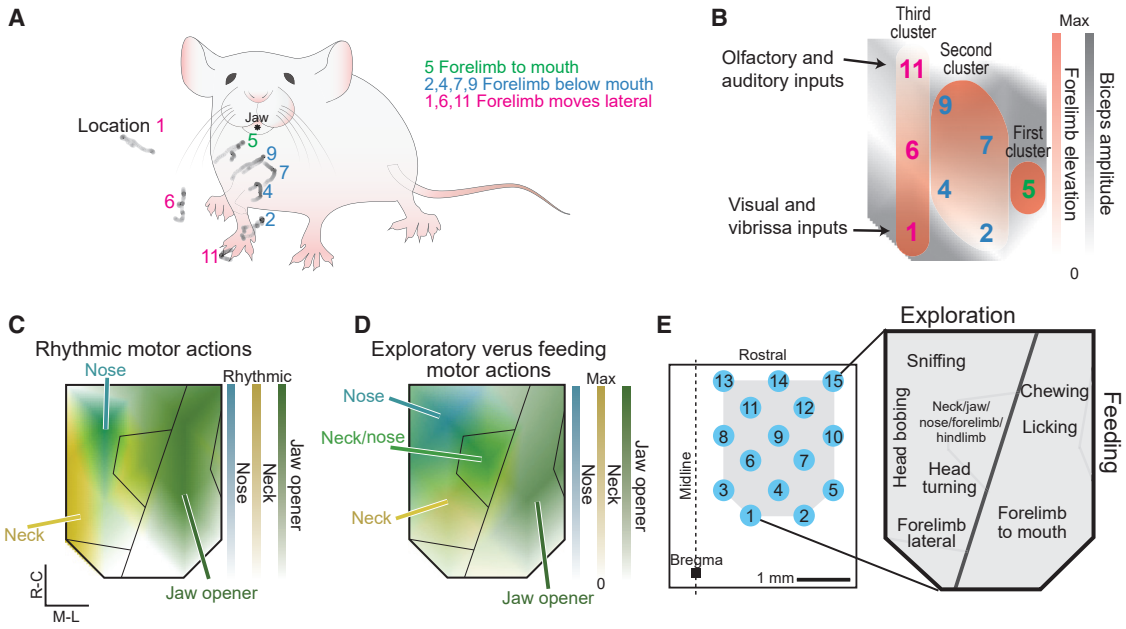

Figure 3. Ethological Orofacial Motor Cortex Map Drawn from Evoked Rhythmic and Ballistic Movements

(A) All evoked forelimb targets (i.e., the black average trace of the projected movements in Figures 2I and S2D) are shown overlaid on an example mouse. The movement from the first cluster is described in green, while the movements from the second and third clusters are shown described in blue and pink, respectively. Location number refers to (B).

(B) Overlay of composite amplitude map of the biceps brachii map (gray; Figure 2F) with the three described clusters of forelimb elevation (red), illustrating that the darker gray locations in MCtx (larger evoked amplitude of biceps brachii) coincide with the darker red stimulation sites in MCtx (higher elevation of forelimb).

(C and D) Overlaid composite maps illustrating the division between exploratory and feeding movements on the basis of rhythmic (C) and ballistic (D) motor actions.

(E) Ethological map of orofacial movements based on Figures 1, 2, and 3.

splenius capitis suggests that this area in MCtx is specialized for head turning (Figures S1A–S1C).

Taken together, the amplitude maps show a patchwork of partially overlapping hotspots that tile across the MCtx and represent unique patterns of muscle activity that cluster according to exploratory versus feeding movements (Figure 1C, inset).

Orofacial Motor Cortex Movement Trajectory Mapping

To advance from maps of individual muscle activation to movement, we measured entire trajectories of the forelimb, jaw, and nose (same five mice as in Figure 1) (Figures 2, 3, and S2A) using videography (Figures 2A–2C). Consistent with the activation of the digastric and masseter muscles (Figure 1F), jaw movements were evoked from most stimulus sites (Figure 2D, filled blue circles). Jaw trajectories were downward and contralateral (Figure 2E). Small movements of the jaw could be detected that corresponded to low-amplitude contractions of the digastric (Figure S2A, location 8). Rhythmic jaw movements (i.e., chewing and licking) were evoked from a subset of locations that had large-amplitude digastric activity (Figures 2E, 2J, and S2A–S2C) and were characterized by rhythmic activation of the digastric (Figures S2B and S2C). As found previously with primates (Huang et al., 1989) and mice (Kobayashi et al., 2002), cortical activation of rhythmic jaw movements can differ slightly from

(E) Jaw movements in two dimensions over time (left) with projected trajectory (right). All trials are shown (colored lines) with the average (black). In the projection, darker lines indicate that more time was spent at those coordinates. The blue box indicates the stimulation duration.

(F) Same as (D), but here filled blue circles indicate locations where visible nose movements were observed, and black outlined circles indicate the example locations for traces in Figure 2G. Movements were similarly observed in three mice.

(G) Nose movements in two dimensions over time (left) and projected trajectory (right). All trials are shown (colored lines) with the average (black). In the projection, darker lines indicate that more time was spent at those coordinates. The blue box indicates the stimulation duration.

(H) Similar to (D) and (F); here filled blue circles indicate locations where forelimb movements were tracked and recorded. Colored outlines indicate which movement type (cluster 1, 2, or 3, as seen in Figures 3A and 3B) was evoked from laser activation at that location. Movements were similarly observed in three mice.

(I) Forelimb movements in two dimensions over time (left) with projected trajectory (right). All trials are shown (colored lines) with the average (black). In the projection, darker lines indicate that more time was spent at those coordinates. The blue box indicates the stimulation duration. An example each for clusters 1 and 2 are shown with the example for cluster 3 in Figure S2D.

(J) Composite maps of locations with rhythmic activity of the digastric (top) and splenius capitis (bottom) muscles along with rhythmic nose movements (middle). Movement descriptions are overlaid. The vibrissa map shows net movement; details are in Figure S1.

natural chewing behaviors in that the masseter is often not rhythmically active, and when it is, the masseter and digastric rhythmic bouts overlap (Figure S2C), as occurs pathologically during bruxism (Taylor et al., 2017). Last, in addition to rhythmic jaw activation, coordinated jaw motor actions were resolved at some stimulation sites. One such movement involved concurrent rhythmic jaw movement with rhythmic protrusion of the tongue (Figure S2A) at a site that was close in location to the previously identified cortical licking region (Komiyama et al., 2010).

Nose movements were elicited by activation of the medial region of MCtx (Figure 2F, filled blue circles). Evoked nose movements were along both the anterior-posterior (Figure 2G, top) and medial-lateral (Figure 2G, bottom) directions. Rhythmic nose movements moved the nose contralaterally and were evoked at only a single stimulus site within the broader region that evoked nose movements (Figures 2G and 2J). The rhythmic activity from the nose was distinct and segregated from that of the jaw (Figure 2J), consistent with known frequencies of chewing, licking, and sniffing in mice as well as their different functions in exploration and feeding (Figure S3A) (Kobayashi et al., 2002; Kurnikova et al., 2017).

It is known that the neck is rhythmically activated during natural chewing (Giannakopoulos et al., 2013; Satoh et al., 2011), sniffing (Kurnikova et al., 2017), and head shakes and bobs (Kobayashi et al., 2002; Kurnikova et al., 2017). Here we found rhythmic activation of the splenius capitis neck muscle at three distinct frequencies, in different regions of orofacial MCtx (Figures 2J and S3A–S3C). The splenius was found to have a similar frequency at locations of digastric rhythmicity to the digastric (Figure S3B, green) and a different frequency that was similar to rhythmic nose movements at locations with nose rhythmicity (Figure S3C, teal). There was a third, slow frequency in medial orofacial MCtx that was independent of other muscles and movements we measured and could, on the basis of frequency, potentially be attributed to head bobbing (Figures S3A–S3C, gold spectra).

The final piece of our cortical map of orofacial movements was to identify evoked forelimb movements (Figures 2H–2J). Although the forelimb is not an orofacial appendage, forelimb movements are an essential aspect of orofacial behaviors such as feeding and grooming. Here, activation of the biceps brachii muscle was induced from all stimulation sites in orofacial MCtx (Figure 1F); however, forelimb movements could only be tracked from stimulation at a subset of sites (Figure 2H, filled blue circles). Three categories of movements were evoked (Figures 2H, 2I, and S2D, green, blue, and pink).

The first forelimb movement type (Figure 2H, location 5; Figures 3A and 3B, first cluster) corresponds to a forelimb trajectory to the mouth with the paw supinated. The elevation of the paw during this evoked movement was higher than for any other evoked movement and was the most closely associated with the mouth (Figure 3A). This stimulation location overlapped with large-amplitude activation of the digastric and large tracked movements of the jaw (Figure 1F). Supination to the mouth was evoked most laterally, within the "feeding" division of orofacial MCtx (Figure 3D).

The second type of forelimb movement (Figures 2I and 2J, locations 2, 4, 7, and 9; Figures 3A and 3B, second cluster of stimulation sites) evoked forelimb grasping below the mouth. These four stimulation sites overlap with the region of strong activation of the splenius capitis and quadriceps muscles (Figure 1F). From the rostral locations of this second cluster (Figures 3A and 3B), evoked forelimb movements that came closer to the face (i.e., more elevated) corresponded with locations that evoked larger jaw opening (Figure 1F), episodically with rhythmic jaw movements (Figure 2H), and larger amplitude responses of the biceps brachii (Figures 1F and 3B).

In the third type of forelimb movement (Figures 2I and S2D, locations 1, 6, and 11; Figures 3A and 3B, third cluster of stimulation sites), the pronated forelimb moved away from the body into the surrounding space (Figure 3A). Less elevated trajectories of this lateral movement were evoked from rostral stimulation sites (Figures 3A and 3B). Activation of the biceps brachii muscle was greatest at locations with larger forelimb elevations (Figure 3B).

We constructed an ethological map of orofacial movements on the basis of overlapping patterns of cortically evoked chewing, sniffing, forelimb-to-mouth movements, head bobbing, head turning, lateral forelimb movements, and licking (Figure 3E). The resulting movements and known cortical inputs support the notion that the medial region of orofacial MCtx is responsible for distinct types of exploratory movements, while more lateral regions are responsible for feeding movements (Figures 3C, 3D, and S3D).

Premotor Distribution in Spinal Trigeminal Subnuclei SpVO and SpVIr

Although MCtx can evoke coordinated movements, it remains unknown if downstream premotor circuits contribute to coordination of these movements. We next determined if trigeminal premotor nuclei have overlapping premotor neuron pools for forelimb, jaw, and vibrissa muscles that could contribute to coordinated movements.

To map the premotor neuron input from muscles of the face and forelimb, we used the transsynaptic retrograde virus pseudorabies at a time point that labeled back to premotor neurons (Matthews et al., 2015). Pseudorabies was chosen for its high efficiency in transporting transsynaptically from muscle in adult animals. To explore coordination of different muscle groups, we chose one muscle from each muscle group of interest: the biceps brachii forelimb muscle, the digastric jaw muscle, and the intrinsic vibrissa muscle (nine mice with three mice per muscle) (Figure 4A). Pseudorabies-labeled neurons were found in both SpVO and SpVIr in all nine mice; example sections for each muscle are shown in Figure 4B. The border between the spinal trigeminal nucleus and the parvocellular reticular formation (PcRt) was determined from the intensity of cytochrome oxidase staining (Furuta et al., 2006) (Figure 4B). Premotor neurons were also found in the adjacent reticular formation and other known premotor regions (Figure 4B).

Consistent with previous literature, more premotor neurons were found in PcRt than in SpVO and SpVIr (Figure S4A, left) (Stanek et al., 2014; Takatoh et al., 2013). Across many animals, a group of neurons that crossed between the PcRt and SpVO was consistently observed (Figure S4B). PcRt neurons appeared to be smaller and denser, while SpVO premotor neurons were

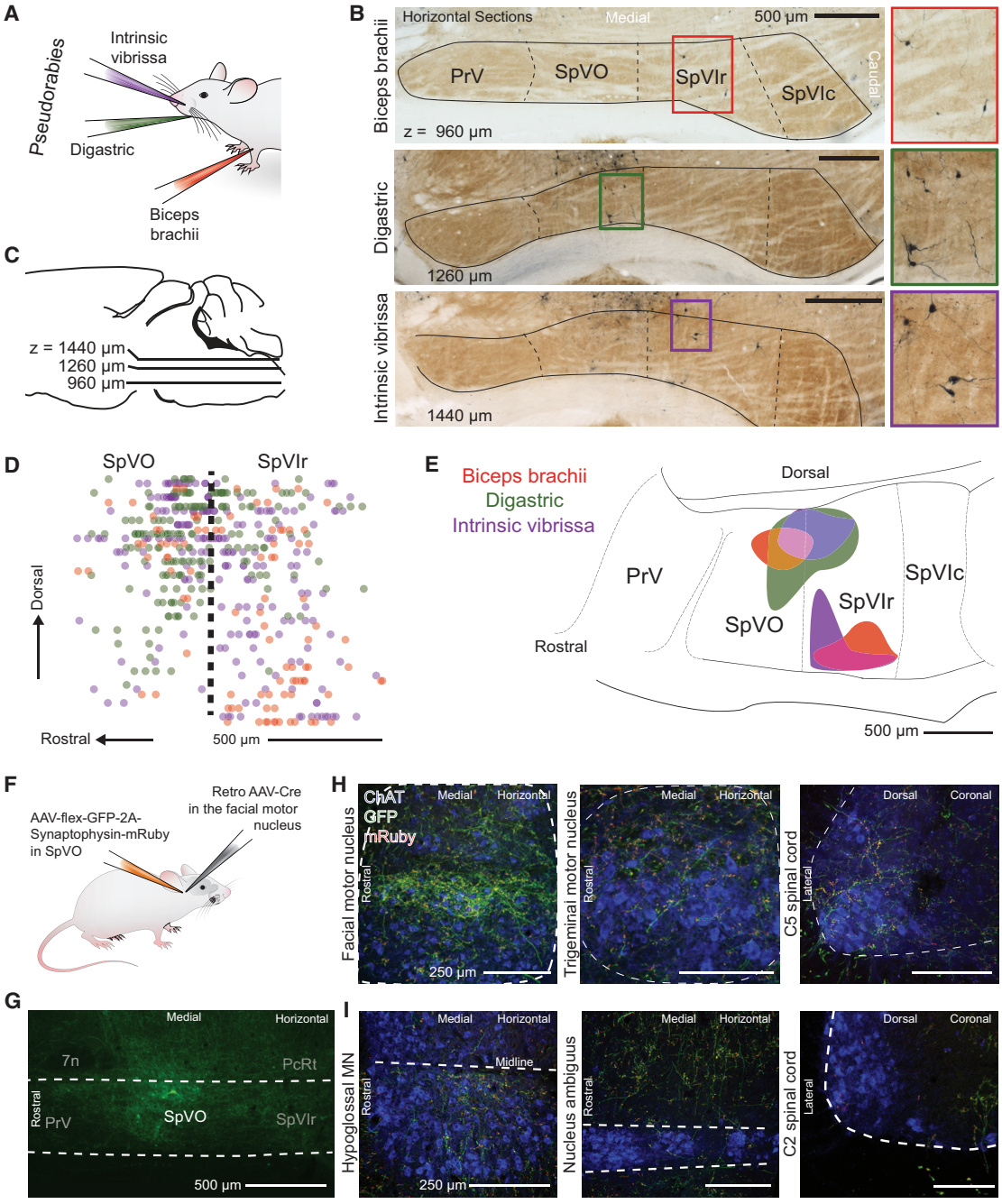

Figure 4. SpVO and SpVIr Have Two Distinct Premotor Neuron Clusters

(A) Schematic illustration of muscle injections of pseudorabies-GFP into the biceps brachii, digastric, and intrinsic vibrissa muscles.

(B and C) Example of horizontal sections from an injection in the biceps brachii, digastric, and intrinsic vibrissa muscles (B), oriented as in (C). GFP was converted to dark product, and sections were counterstained with cytochrome oxidase.

(D) Sagittal reconstruction of all premotor labeled neurons in SpVO and SpVIr.

(E) Two clusters found using the 50% densest labeling of digastric and biceps premotor neurons and 42% of intrinsic premotor neurons in SpV are overlaid on a sagittal atlas section (Paxinos and Franklin, 2008); see STAR Methods. SpVO cluster has 14 biceps, 88 digastric, and 57 intrinsic vibrissa premotor neurons. SpVIr cluster has 33 biceps, 1 digastric, and 34 intrinsic vibrissa neurons. Total premotor neurons was 94 biceps, 178 digastric, and 218 intrinsic vibrissa premotor neurons across nine mice.

(F) Schematic illustration of the injection scheme for a Cre-dependent AAV with somatic GFP and synaptophysin-mRuby into SpVO and a retrograde AAV-Cre into the facial motor nucleus.

(legend continued on next page)

bigger with more elaborate dendrites (Figure S4B). Prior literature also suggested PrV as an important premotor structure for jaw rhythmicity (Tsuboi et al., 2003). With pseudorabies labeling, we found that SpVO and SpVIr had more labeled premotor neurons than PrV (Figure S4A, middle panel). The tropism of pseudorabies is unknown, but in a subset of mice, very dense labeling was found in nociceptive-related substructures in SpVC (Figure S4A, right panel), leading to large variability in the number of pseudorabies-labeled neurons present there (Figure S4C). Although there are many premotor neurons in the reticular formation, the somatotopy, distinct subdivisions, and raw sensory input make the trigeminal complex an ideal location to examine for coordination of motor control (three additional mice were included in the Supplemental Information).

We reconstructed the labeled neurons from SpVO and SpVIr in three dimensions and projected them onto the sagittal plane (Figure 4D). The top 50% densest labeled neurons (Figure 4E) formed two clusters of premotor neurons. The first cluster is in the dorsal part of SpVO, and the second is in the ventral part of SpVIr. The dorsal cluster in SpVO receives somatosensory information for the jaw, inside the mouth, and the teeth (Jacquin and Rhoades, 1990; Yoshida et al., 1994) and was found to have premotor neurons for all three muscles: the biceps brachii digastric and intrinsic vibrissa muscles. The ventral premotor cluster in SpVIr receives sensory input from the face around the eyes, the nose, and the vibrissae (Jacquin et al., 1986) and has a more selective premotor neuron population for only the biceps brachii and intrinsic vibrissa muscles. The distinction between the premotor clusters and the known sensory topography suggests that these clusters are part of separate circuits (Figures 4D and 4E).

To further understand the nature of the pathway from MCtx to muscles, we sought to determine if individual premotor neurons in the trigeminus send collateral axons to motoneurons in different cranial nuclei and the spinal cord. We injected a Cre-dependent virus that labeled the axons with GFP and the presynaptic terminals with mRuby into SpVO (Figures 4F, 4G, and S5A), while injecting a retrograde AAV-Cre virus into the facial motor nucleus (Figure 4H, left panel; Figure S5A), the location of vibrissa, nose, and other face motoneurons (five mice). Collateral terminals were observed in the trigeminal motor nucleus, the location for most jaw opening and closing motoneurons (masseter and anterior digastric motoneurons; Figure 4H, middle panel; Figure S5B), and in the ventral horn motor neurons in the lower cervical spinal cord, (Figure 4H, right panel; Figure S5B), at approximately the level where forelimb motor neurons are found. Across animals, more terminals were observed within the facial motor nucleus than the trigeminal motor nucleus or the ventral horn of the spinal cord (Figure S5B). However, the effective strength of individual connections remains unknown.

These data provide anatomical evidence for functional coordination of motor actions by the face, forelimb, and jaw via single premotor neurons in SpVO. Additional collateral terminals were observed in the hypoglossal motor nucleus while mostly avoiding the nucleus ambiguus and the ventral horn in the upper cervical spinal cord (Figure 4I), which suggests that although some overlap among premotor pathways is present, the pathways are targeting a distinct subset of motoneuron pools. Together, these data show that overlapping pathways from premotor to motoneurons can be through the same premotor neurons. They build on prior claims that individual premotor neurons contact motoneurons in different cranial nuclei and within the spinal cord (Li et al., 1993; Stanek et al., 2014; Yoshida et al., 1994).

A final point concerns the range of input from orofacial MCtx to SpVO and SpVIr. We used a retrograde lentivirus-Cit (Figure S6A) to label cortical neurons that projected to either dorsal SpVO (Figure S6B, top) or ventral SpVIr (Figure S6B, bottom panel). A three-dimensional reconstruction (Figure S6D) shows that for each viral injection in either dorsal SpVO or ventral SpVIr, neurons in MCtx were identified from the rostral pole to bregma and the entire mediolateral extent of AG_m and AG_l cortex (Figure S6D). Similar results were found in all retrogradely labeled animals (11 mice contributed to the Supplemental Information). In addition, labeling from both dorsal SpVO and ventral SpVIr was seen across primary sensory somatosensory cortex (Figure S6D).

Density Analysis of Motor Cortex Inputs

The density of axonal boutons from MCtx to premotor regions is roughly constant for injection sites across MCtx (Alloway et al., 2010; Jeong et al., 2016). Yet the distribution of inputs within the trigeminal subnuclei has not been quantified (Alloway et al., 2010). To form such a map, we first injected an anterograde lentivirus-synaptophysin-GFP virus that specifically labels presynaptic endings (Figures 5A–5C) in three locations across the mediolateral axis of MCtx (Figure 5D; three mice). The distribution of boutons was reconstructed in three dimensions and then projected in the sagittal plane (Figure 5E). The medial injections projected most densely to ventral SpVO and SpVIr (Figure 5F). As the injections progressed toward the AG_l cortex, the density shifted to the dorsal region of SpVO and SpVIr (Figures 5E and 5F). This distinction in density suggests that the MCtx differentially targets the dorsal, jaw sensory region, and the ventral, vibrissa and nose sensory region of SpVO and SpVIr depending on the mediolateral location in MCtx, further supporting the medial-exploratory and lateral-feeding division suggested from Figures 1, 2, and 3.

The caudal part of the AG_m cortex is known to be innervated by primary visual and somatosensory cortices (Barthas and Kwan, 2017; Hoffer et al., 2003; Wang and Burkhalter, 2007), whereas the more rostral region is innervated by the auditory cortex (Donoghue and Parham, 1983; Reep et al., 1987). We next tested if there was a bias in the density of projections from these different

(G) Image of GFP labeling at the anterograde injection site in SpVO.
(H) Images of axon and terminal labeling in the retrograde injection site of the facial motor nucleus (left) and of collateral axons and terminals in the trigeminal motor nucleus (middle) and the lower cervical spinal cord (right).
(I) Example section of terminal labeling in the hypoglossal motor nucleus (left) and lack of labeling in the region of motor neurons in the nucleus ambiguus (middle) and the upper cervical spinal cord (right).

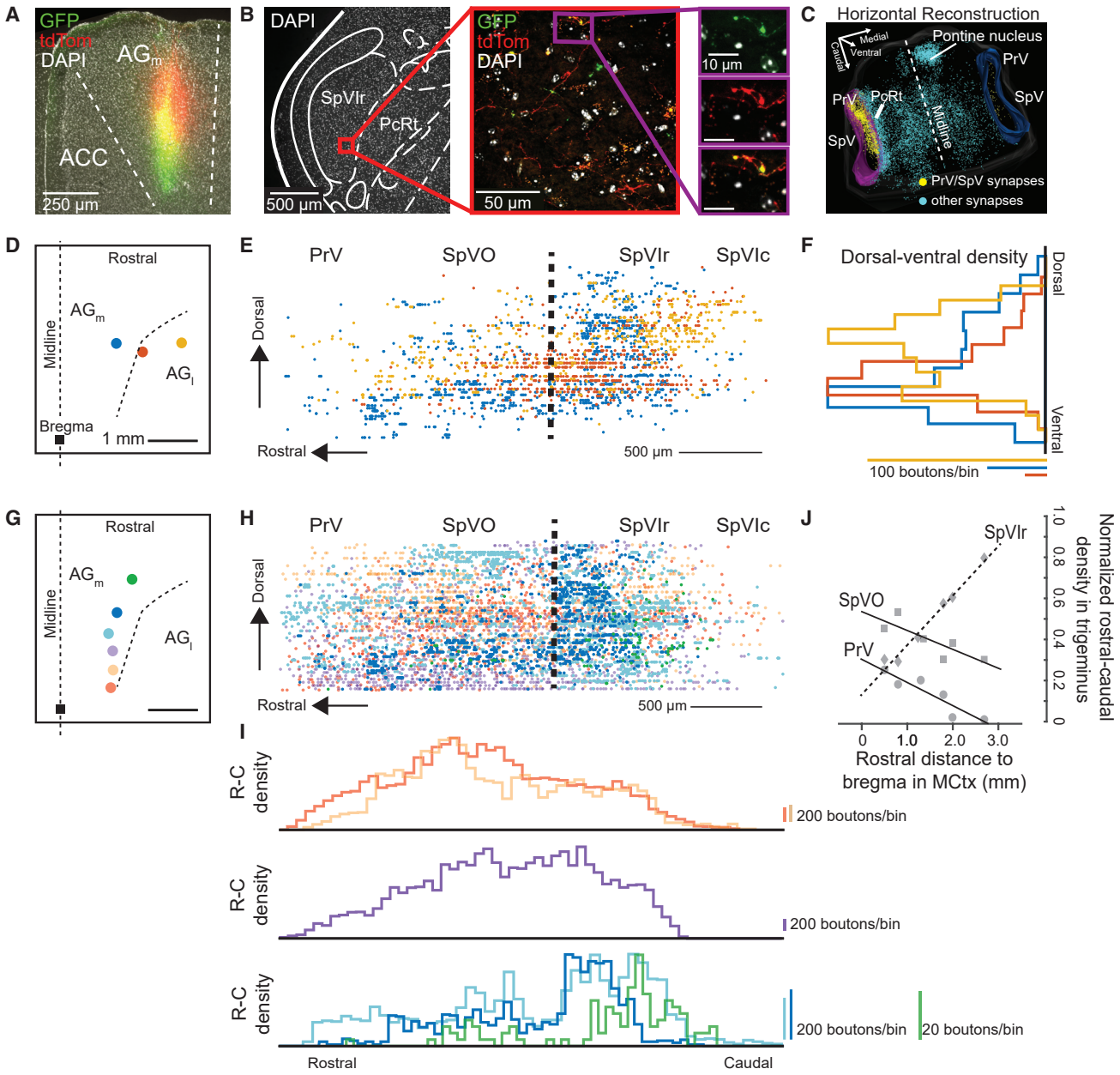

Figure 5. Density of Inputs from Motor Cortex Biases within the Spinal Trigeminal Complex Dependent on Cortex Location

(A) Lentivirus-CAG-synaptophysin-eGFP coinjected with AAV-hSyn-tdTomato in the AG_m region of MCtx. No spill was found in anterior cingulate cortex (ACC).

(B) Synapses (green and red) and axons (red only) labeled in SpVIr from (A).

(C) Three-dimensional (3D) reconstruction of GFP-labeled boutons of the hindbrain viewed from above.

(D) Schematic of MCtx injections in AG_m and lateral to AG_l; the square represents bregma. Each colored circle corresponds to one injection in one mouse.

(E) Sagittal projection of synapses labeled rostrally from PrV through SpVIc caudally color coded by injection site in panel D (4,848 synapses across three mice).

(F) Overlaid histograms of dorsal-ventral density in PrV through SpVIc for injections in AG_m and AG_l; scaling information shown below.

(G) Schematic of MCtx injections in AG_m that run along the rostral-caudal axis. Each dot corresponds to one mouse.

(H) Sagittal projection of synapses labeled rostrally from PrV through SpVIc caudally color coded by injection site in (F) (17,226 synapses across six mice). Some datasets were down-sampled for clarity.

(I) Histograms of rostral-caudal density from color-coded injection sites in (G), scaling information shown on the right.

(J) Plot of percentage synaptic density in PrV, SpVO, and SpVIr out of all trigeminal synapses (PrV + SpVO + SpVIr + SpVIc) as the injections move rostral from bregma.

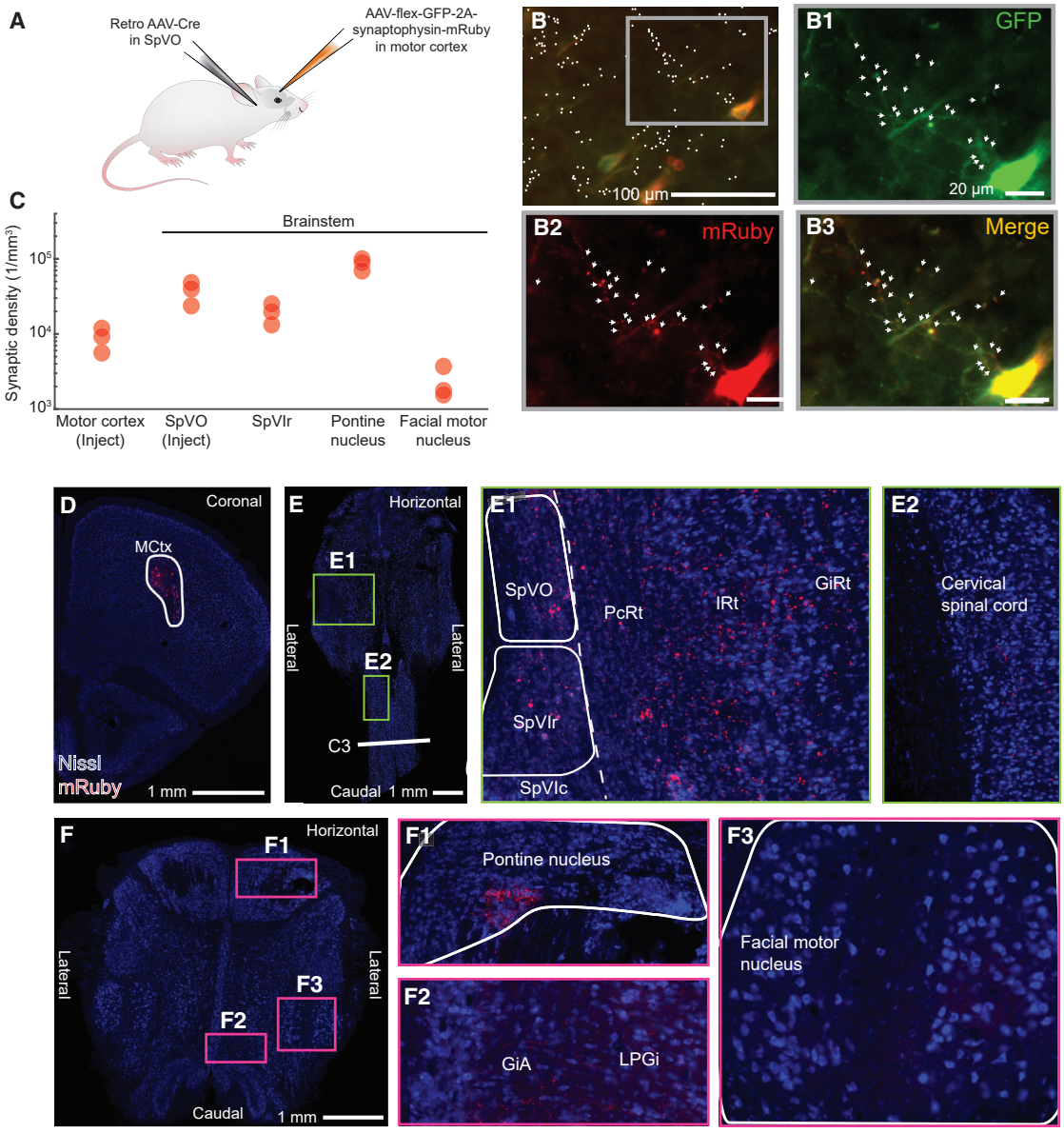

Figure 6. Motor Cortex Collaterals Broadly Target Brainstem Premotor Nuclei

(A) Injection scheme for collateral labeling with a retro AAV-Cre injected in SpVO and AAV-flex-GFP-2A-synaptophysin-mRuby in MCtx.

(B) Pyramidal neurons (red and green) and labeled axons (green) and synapses (red and green) labeled by AAV-flex-mGFP-2A-synaptophysin-mRuby. White dots (left top image) indicate counted synapses with arrows (three enlarged images) showing co-labeling at synapses. Motor cortex injection coordinates: bregma + 3.0, 2.0 lateral.

(C) Quantification of synaptic density in MCtx, pontine nucleus, facial motor nucleus, SpVO, and SpVlr (50,473 boutons and 135 cells across three mice). See white outlines of MCtx injection, SpVO, SpVlr, the facial motor nucleus, and the pontine nucleus (D–F) for areas used for density calculation.

(D) Large view of MCtx injection site described in (A) with white outline used for density calculation.

(E) Retrograde injection into SpVO shown with collaterals found in SpVlr (E1), the medullary reticular formation (E1), and the cervical spinal cord (E2). White outlines for SpVO and SpVlr used in density calculation.

(F) Collaterals of SpVO-projecting MCtx neurons in the pontine nucleus (F1), the alpha part of the gigantocellular reticular formation (F2), the lateral paragigantocellular reticular formation (F2), and the facial motor nucleus (F3).

parts of AG_m through a series of injections on the rostral-caudal axis (Figure 5G; one of the three original plus five additional mice). Here we found that injections into rostral AG_m projected most densely to SpVlr, and, as the injections were more caudal, the projections shift toward SpVO (Figures 5H–5J). This finding is further confirmed by examining the rostral-caudal terminal density from the medial-lateral MCtx injections (Figures 5D–5F); all injections were made at approximately the same rostral-caudal

coordinates. We find that all the resulting terminal densities in the trigeminus have their major peak in the same approximate rostral-caudal location in SpVIr (Figure S6E).

In toto, we observe two distinct gradients formed from MCtx inputs to SpVO and SpVIr. Medial-lateral injections shift the inputs ventro-laterally (Figure 5F), while rostral-caudal injections shift the inputs caudal-rostrally (Figures 5I and 5J). These data suggest that although MCtx projects broadly to these nuclei, one mechanism of movement specialization could be determined by gradients of cortical inputs.

Motor cortex corticofugal neurons are known to have broad axonal collateralization across the brainstem (Economo et al., 2018; Kita and Kita, 2012). As such, we asked if SpVO and SpVIr receive collaterals from the same neurons in MCtx. We injected a Cre-dependent AAV into MCtx and a retrograde AAV-Cre into SpVO (Figure 6A). We observed boutons in SpVIr (Figures 6B and 6C) in all animals (eight mice, five from vibrissa MCtx [AP +1.5, ML 1.5] and three from jaw MCtx [AP +3.0, ML 2.0]). This shows that the same corticobulbar cell projects to two distinct regions of the spinal trigeminal nucleus, although likely not with the same density (Figure 5).

Given that the distinction between the SpVO and SpVIr premotor clusters concerns their projections to jaw motoneurons, we analyzed the projections from MCtx neurons that were located where rhythmic jaw movements were consistently observed (AP +3.0, ML 2.0; Figure 3B). We determined the density of collateral inputs to both SpVO and SpVIr premotor neuron populations as well as local collaterals within MCtx (Figures 6B and 6C). We labeled pyramidal neurons in MCtx by the intersection of a Cre-dependent AAV injected into MCtx and retrograde AAV-Cre into SpVO (Figure 6A); pre-synaptic terminals were labeled with mRuby and expressed somatic GFP (Figures 6B–6F and S7A–S7E). Distinct brainstem collateral projections were observed in the pontine nucleus, superior colliculus, periaqueductal gray, spinal cord, and reticular formation, that is, parvicellular reticular formation (PcRt), intermediate reticular formation (IRt), gigantocellular reticular formation (GiRt), the alpha part of the gigantocellular reticular formation (GiA), the lateral paragigantocellularis (LPGi), and midbrain reticular formation (Figures 6E, 6F, and S7C–S7E). Fibers were seen consistently in the VM and CM thalamic nuclei (Figure S7B), and sparse fibers were seen in primary somatosensory cortex (Figure S7B) and the facial motor nucleus (Figure 6F). To quantify the strength of the relative projections, we counted the number of boutons formed by axon collaterals of SpVO-projecting MCtx neurons in a known dense target (i.e., the pontine nucleus), a known weak target (i.e., the facial motor nucleus) (Grinevich et al., 2005), the retrograde injection site SpVO, SpVIr, and within the anterograde injection site in MCtx (Figures 6D–6F). The density was estimated on the basis of labeled outlines for MCtx, SpVO, SpVIr, pontine nucleus, and facial motor nucleus (Figures 6D–6F). We confirm a strong collateral projection to the pontine nucleus, with 7 times the density seen in MCtx, and a weak collateral to the facial motor nucleus, with 0.2 times of MCtx (Alloway et al., 2010; Grinevich et al., 2005; Kita and Kita, 2012) (Figure 6C). With regard to collateral activation of neighboring cortical neurons near the injection site in MCtx, we found that the density of boutons is 4 times higher in SpVO than within MCtx (Figure 6C).

Taken together, the data from our anatomical studies (Figures 4, 5, and 6) confirm that SpVO and SpVIr are both premotor and receive input from MCtx. The patterns of connectivity are found as gradients of inputs from cortex to the trigeminal nuclei along two directions (Figure 5J) and both SpVO and SpVIr receive collaterals from the same corticobulbar neurons (Figures 6C and 6E). Notably, both the MCtx neurons that project to the trigeminal complex (Figure 6) and the premotor neurons from SpV to the facial motor nucleus (Figures 4F–4I) have many collaterals that project to arrays of motor nuclei. This creates a parallel set of connections that may be co-activated by cortical neurons.

Optogenetic Activation of SpVO- and SpVIr-Projecting MCtx Neurons

We now address how an isolated corticobulbar pathway contributes to coordination of motor actions. We used a transectional virus strategy to label SpVO- or SpVIr-projecting MCtx neurons with a red-shifted channelrhodopsin (Lin et al., 2013). We then tested if stimulation of SpVO- and SpVIr-projecting MCtx neurons activated distinct sets of muscles, consistent with their respective, distinct populations of premotor neurons (Figure 4E). AAV retro-Cre was injected into either SpVO or SpVIr (Figures 7A, 7B, S7F, and S7G), while AAV-flex-ReaChR-Cit was injected into two cortical locations (Figure 7C), one that in Thy1-ChR2 mice evoked rhythmic jaw movements and a second in vibrissa MCtx (Figure 2J). After the viruses expressed, mice were head-fixed, and a scanning laser system was used to selectively stimulate a discrete region within each injection site in MCtx with a 10 Hz, 10 s long train of pulses of red light (Figures 7A–7C). We concurrently recorded EMGs from the biceps brachii, digastric, intrinsic vibrissa, masseter, and splenius capitis muscles and observed robust single-trial responses (Figures 7A and 7D).

Prolonged, localized stimulation of cortex in mice with labeled SpVO-projecting MCtx neurons led to concurrent activation of the biceps brachii, digastric, intrinsic vibrissa, and masseter muscles (Figures 7E and 7F). Averaged across animals (three mice), there was statistically equal activation across all muscle groups for stimulation at a given site ($p > 0.1$, ANOVA) (Figure 7G; colors indicate significant responses from baseline, while gray indicates insignificant responses).

In contrast to the result for SpVO-projecting MCtx neurons, stimulating SpVIr-projecting MCtx neurons reliably activated only the biceps brachii and intrinsic vibrissa muscles (Figures 7H and 7I). Critically, there was a significant and notable lack of evoked activity in either jaw muscle, a result that held across all animals (three mice) and from both stimulus sites (Figure 7J). A final point is that SpVO-projecting MCtx neurons from the "vibrissa" site evoked larger amplitude movements than from the "jaw" site (Figure 7G), while SpVIr-projecting MCtx neurons in the "jaw" site evoked larger movements than from the "vibrissa" site (Figure 7J). This is consistent with the result that SpVO receives a denser cortical input from more caudal MCtx locations and SpVIr receives a denser cortical input from more rostral MCtx locations (Figure 5J).

The reduced expression of channelrhodopsin with viral labeling versus expression in Thy1-ChR2 mice necessitated the use of prolonged stimulation. Rhythmic and ballistic movements

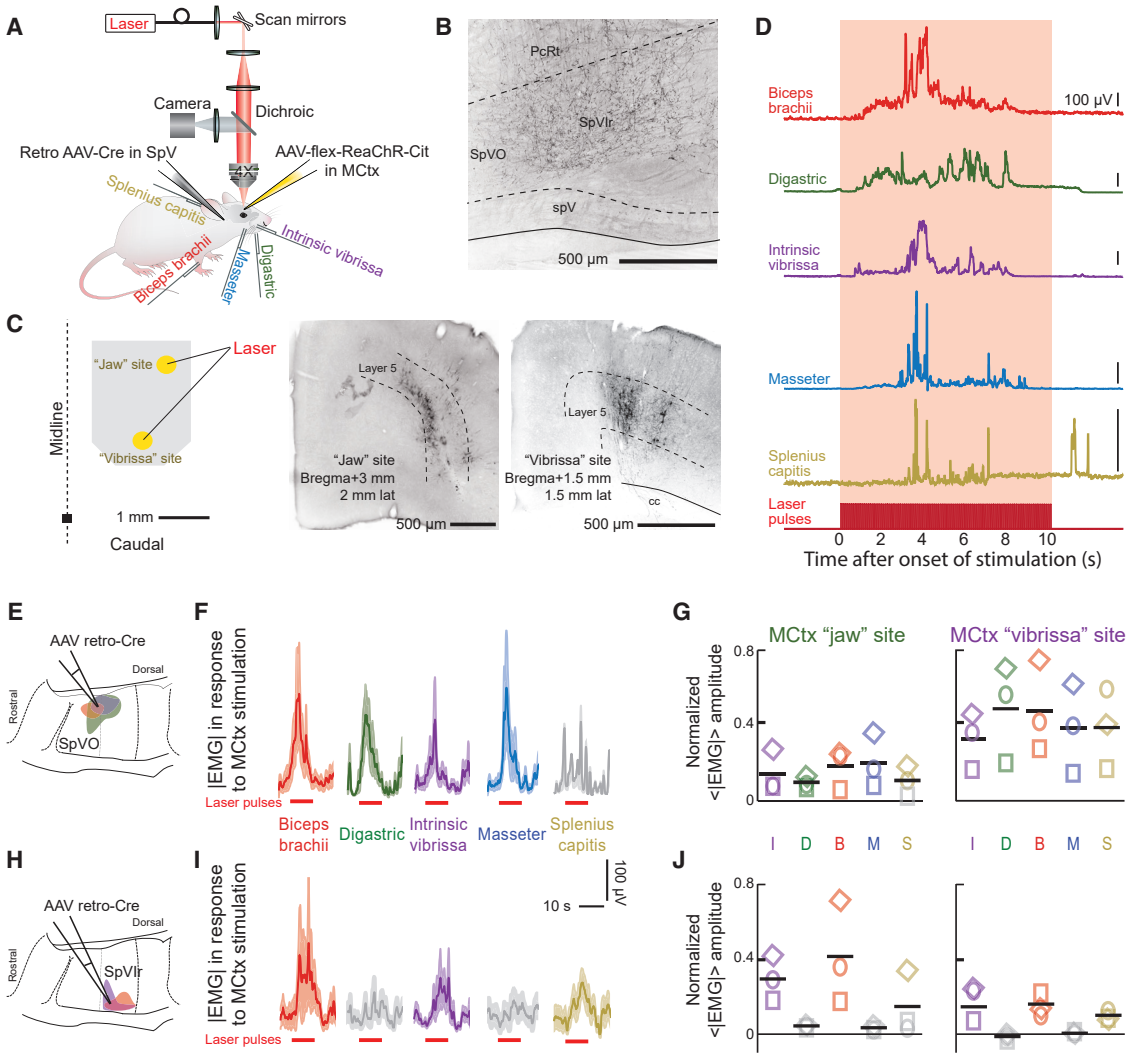

Figure 7. SpVO- and SpVIr-Projecting Motor Cortex Neurons Drive Different Networks that Activate Muscles Reflecting Their Respective Premotor Clusters

(A) Schematic illustrating the injection scheme as well as the later used red laser and recorded EMGs in the bicep brachii, digastric, intrinsic vibrissa, masseter, and splenius capitis muscles.

(B) Axon terminals in SpVIr, an example of a retrograde AAV-Cre injection site.

(C) Schematic of injection site and corresponding laser size (left). Cortex injection "jaw" site coordinates: bregma + 3.0, 2.0 lateral. Cortex injection "vibrissa" site coordinates: bregma + 1.5, 1.5 lateral. Virus-labeled pyramidal neurons from a jaw MCtx and a vibrissa MCtx injection (middle and right, respectively).

(D) Envelopes of the EMG signal for the biceps brachii, digastric, intrinsic vibrissa, masseter, and splenius capitis muscles for a single trial. Note that the intertrial interval was 50 s.

(E–G) Activation of EMGs using AAV retro-Cre targeted to the SpVO premotor cluster (E). Stimulus-triggered averages and standard deviations from stimulation the MCtx "jaw" site (F) and averages across mice (G) from jaw MCtx (left) and vibrissa MCtx (right) (10–20 measurements per muscle per cortex location across three mice). Gray traces in (F) or symbols in (G) show insignificant responses ($p < 0.05$, Student's t test).

(H–J) Activation of EMGs using AAV retro-Cre targeted to the SpVIr premotor cluster (H). Stimulus-triggered averages and standard deviations from stimulation of the MCtx "jaw" site (I) and averages across mice (J) from jaw MCtx (left) and vibrissa MCtx (right); 10–20 measurements per muscle per cortex location across three mice.

have been shown to be continuously evoked throughout a cortical stimulation for durations up to 10 s (Graziano and Aflalo, 2007; Huang et al., 1989; Isogai et al., 2012; Lund et al., 1984). Nonetheless, we compared the response for blue light with Thy1-ChR2 animals versus red light with virus-expressed ReaChR animals using 10 s stimuli at the same stimulation location in MCtx (Figure S7H). Qualitatively similar EMG responses are seen for the vibrissa intrinsic and digastric muscles, with the exception that stimulation of SpVIr-projecting MCtx neurons do not drive the digastric muscle (Figure 7J).

These stimulation data, in combination with the mapping data of trigeminal subnuclei to different motoneurons pools (Figures

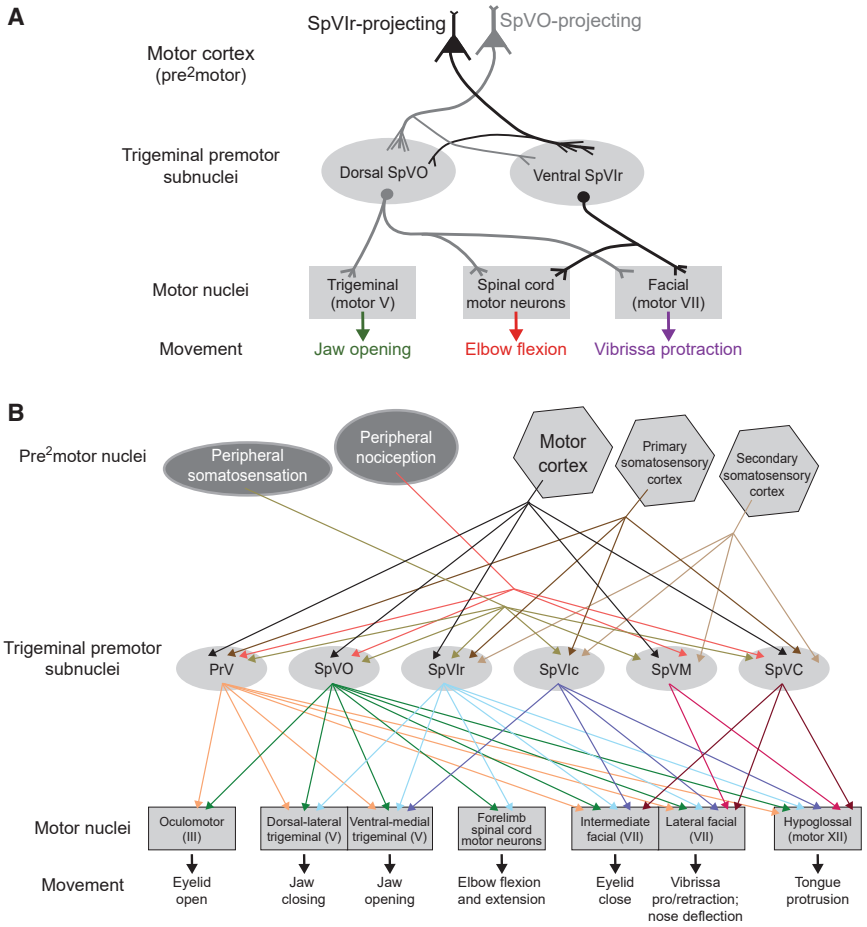

Figure 8. Model and Summary

(A) Model summarizing the activation with the anatomical data from Figures 5, 6, and 7. There are two distinct premotor clusters, one in SpVO and another in SpVIr. When activating cortical projection neurons targeting either SpVO or SpVIr, resulting muscle activation reflects the premotor neurons in the targeted cluster.

(B) Summary of published data, as well as data from this manuscript, on the connectivity from premotor areas, including peripheral (Bereiter et al., 2000; Capra and Dessem, 1992; Furuta et al., 2006; Ren and Dubner, 2011; Sabino et al., 2002; Sakurai et al., 2013; Yoshida et al., 1994) and cortical (Smith et al., 2015; Sreenivasan et al., 2015) areas, through all trigeminal premotor areas to distinct motor neurons (Borke et al., 1983; Erzurumlu and Killackey, 1979; Esposito et al., 2014; Kurnikova et al., 2019a; Li et al., 1995; May et al., 2012; Pinganaud et al., 1999; Stanek et al., 2014; Takatoh et al., 2013; van Ham and Yeo, 1996). See tab for Figure 8B in Table S2 for a link of publications to specific pathways.

4E and 4H), highlight that motor control is in part set by premotor neurons and not strictly by neurons in MCtx (Figure 8A). Taken altogether, our data show that MCtx corticobulbar pathways have specific contacts at the premotor level with premotor neurons in control of certain aspects of movement and thus coordination of orofacial movements is controlled at the premotor level as well as the MCtx (Figures 8A and 8B).

DISCUSSION

We observed that ethologically relevant movements were tiled across orofacial MCtx (Figures 1, 2, and 3). The combined results from anatomical (Figures 4, 5, and 6) and cortical activation (Figure 7) studies support the presence of two distinct circuits that originate from the same locations in cortex and act, in part, through identified clusters of premotor neurons in trigeminal subnuclei SpVO and SpVIr. Activation of either pathway drove the forelimb and vibrissa muscles (Figures 7E–7J), while jaw movements occurred only from activation of SpVO-projecting MCtx neurons (Figures 7E–7G). These different patterns occur even though both SpVO and SpVIr receive collateral input from the same MCtx neurons (Figures 6C and 6E). We thus conjecture that neighboring corticobulbar projections neurons from MCtx form synapses on specific subsets of neurons in each trigeminal target. These feedforward circuits then drive specific combinations of motor actions that involve the forelimb, head, jaw, and vibrissa (Figures 3G and 8A).

The corticobulbar inputs to the trigeminus are broadly distributed in the form of spatial gradients (Figure 5). The data on projections from localized regions in MCtx to the trigeminus (Figure 5) reveal a newfound organization of the cortical activation of trigeminal premotor nuclei. When we activated one of two distinct locations in MCtx that selectively targets SpVO versus SpVIr (Figure 7), the strength of the evoked amplitudes of muscle activity reflects the gradients of input; that is, larger amplitude responses occurred for regions of denser corticobulbar connections (Figures 5J, 7G, and 7J).

One caveat to this study is the reliance on viral methods. Although viruses show very clear labeling of axons and can be used to encode opsins, they, like traditional tracers, can spread beyond the intended injection target. As such, we purposely show injection sites for example data and include measures of the spread of the injected virus (Figures S5A and S7F). Furthermore, electrophysiological recording was used to identify these target structures for injections. For anterograde injections into SpVO (Figures 4G and S5A), all neurons were identified to be within SpVO. For retrograde injection sites into SpVO and SpVIr (Figures 6A and 6E), it was difficult to identify the spread, as there are collateral axons in many of the neighboring structures. It is possible that some spill occurred, most likely into the PcRt, as the spinal trigeminal nucleus is most narrow in the medial-lateral dimension.

Altogether, our data highlight the distributed nature of the coordination of motor actions into behaviors along both the MCtx to trigeminus projections and the trigeminus to motoneuron projections (Figure 8A). Although we focused on two

subpathways from MCtx, we also confirmed the previously reported existence of broad collateralization (Figure 6). It is important to note that all the stimulation experiments (Figure 7) were simultaneously activating the trigeminal nucleus targeted with the AAV-retro Cre (i.e., SpVO or SpVIr), as well as the collateral targets of those corticobulbar neurons (Figure 6). Furthermore, the complexity of activation continued as the premotor neurons acted on all their collaterals (Figures 4G and 4H). Notably however, in both the stimulation of the Thy1-ChR2 mice (Figures 1, 2, and 3) and virus-encoded ReaChR mice (Figure 7), the activity patterns were consistent across short (i.e., 1 s) versus long (i.e., 10 s) stimulation (Figures 2 and 7). This result indicates that corticobulbar neurons engage entire networks and that multiple corticobulbar and corticospinal networks work together to piece different movements into behaviors.

One feature of the trigeminus is the convergence of peripheral sensory input, including input related to self-motion of the sensors (Nguyen and Kleinfeld, 2005; Bellavance et al., 2017) as well as nociception (Capra and Dessem, 1992; Sabino et al., 2002), with input from higher order cortical centers (Kleinfeld et al., 1999; Bosman et al., 2011; McElvain et al., 2018). This includes input from MCtx along with primary and secondary somatosensory cortices (Smith et al., 2015; Sreenivasan et al., 2015) to premotor neurons (Figure 8B). Although rodent MCtx targets many premotor nuclei, the trigeminal complex is unique in receiving an abundance of somatosensory information in addition to motor information. The pattern of connectivity from premotor neurons in the trigeminal complex to muscle groups that span different motor nuclei has the form of a highly divergent feedforward network. Going forward, the more far reaching goal would be to identify the specific role of different collaterals from corticobulbar and corticospinal neurons. Conditional expression of Cre transsynaptic from neurons in MCtx, a potential emerging technology (Lo and Anderson, 2011), should enable us to parse these connections. At the intersection of motor and sensory, the trigeminal nuclei have the potential to be an ideal location to begin this process (Figure 8B).

STAR★METHODS

Detailed methods are provided in the online version of this paper and include the following:

- KEY RESOURCES TABLE
- LEAD CONTACT AND MATERIALS AVAILABILITY
- EXPERIMENTAL MODEL AND SUBJECT DETAILS
  - Mice
- METHOD DETAILS
  - Muscle Injections
  - Brain Injections
  - Headbar Placement
  - Optogenetic Stimulation Experiments
  - Histology
  - Computational Analyses
- QUANTIFICATION AND STATISTICAL ANALYSIS
  - Statistical Tests
  - Quantification
- DATA AND CODE AVAILABILITY

SUPPLEMENTAL INFORMATION

Supplemental Information can be found online at https://doi.org/10.1016/j.neuron.2019.08.032.

ACKNOWLEDGMENTS

We thank Martin Deschênes, Beth Friedman, Josh Huang, Takaki Komiyama, Celine Matéo, Lauren McElvain, and Fan Wang for discussions; Grégory Scherrer for the use of reagents; Agnieszka Brzozowska-Prechtl for assistance with histology; and Beth Friedman for assistance with the manuscript. This work was supported by NIH grants NS058668, NS0905905, and NS097265. The Neuroscience Microscopy Imaging Center was supported by NIH grant NS047101 and gift funds through the University of California (UC), San Diego, School of Medicine.

AUTHOR CONTRIBUTIONS

H.J.K., P.M.K., D.K., and N.M.L. planned the experiments. D.G. and A.F.L. prepared viral reagents. P.M.K. and D.K. designed the apparatus. P.M.K. wrote the acquisition software. N.M.L. performed all experiments and data analysis. D.K. and N.M.L. prepared figures and wrote the manuscript. D.K. attended to the myriad university rules and forms that govern environmental health and safety, including the ethical use of animals, as well as the use of chemicals, controlled substances, hazardous substances, lasers, and viruses.

DECLARATION OF INTERESTS

The authors declare no competing interests.

Received: March 4, 2019
Revised: July 7, 2019
Accepted: August 19, 2019
Published: October 3, 2019

REFERENCES

Alloway, K.D., Smith, J.B., and Beauchemin, K.J. (2010). Quantitative analysis of the bilateral brainstem projections from the whisker and forepaw regions in rat primary motor cortex. J. Comp. Neurol. *518*, 4546–4566.

Amri, M., Car, A., and Roman, C. (1990). Axonal branching of medullary swallowing neurons projecting on the trigeminal and hypoglossal motor nuclei: demonstration by electrophysiological and fluorescent double labeling techniques. Exp. Brain Res. *81*, 384–390.

Amundsen Huffmaster, S.L., Van Acker, G.M., 3rd, Luchies, C.W., and Cheney, P.D. (2017). Muscle synergies obtained from comprehensive mapping of the primary motor cortex forelimb representation using high-frequency, long-duration ICMS. J. Neurophysiol. *118*, 455–470.

Arenkiel, B.R., Peca, J., Davison, I.G., Feliciano, C., Deisseroth, K., Augustine, G.J., Ehlers, M.D., and Feng, G. (2007). *In vivo* light-induced activation of neural circuitry in transgenic mice expressing channelrhodopsin-2. Neuron *54*, 205–218.

Barthas, F., and Kwan, A.C. (2017). Secondary motor cortex: where 'sensory' meets 'motor' in the rodent rrontal cortex. Trends Neurosci. *40*, 181–193.

Bellavance, M.-A., Takatoh, J., Lu, J., Demers, M., Kleinfeld, D., Wang, F., and Deschênes, M. (2017). Parallel inhibitory and excitatory trigemino-facial feedback circuitry for reflexive vibrissa movement. Neuron *95*, 673–682.e4.

Bereiter, D.A., Hirata, H., and Hu, J.W. (2000). Trigeminal subnucleus caudalis: beyond homologies with the spinal dorsal horn. Pain *88*, 221–224.

Bonazzi, L., Viaro, R., Lodi, E., Canto, R., Bonifazzi, C., and Franchi, G. (2013). Complex movement topography and extrinsic space representation in the rat forelimb motor cortex as defined by long-duration intracortical microstimulation. J. Neurosci. *33*, 2097–2107.

Borke, R.C., Nau, M.E., and Ringler, R.L., Jr. (1983). Brain stem afferents of hypoglossal neurons in the rat. Brain Res. *269*, 47–55.

Bosman, L.W.J., Houweling, A.R., Owens, C.B., Tanke, N., Shevchouk, O.T., Rahmati, N., Teunissen, W.H.T., Ju, C., Gong, W., Koekkoek, S.K.E., et al. (2011). Anatomical pathways involved in generating and sensing rhythmic whisker movements. Frontiers in Integrative Neuroscience. Published online October 3, 2011. https://doi.org/10.3389/fnint.2011.00053.

Brecht, M., Krauss, A., Muhammad, S., Sinai-Esfahani, L., Bellanca, S., and Margrie, T.W. (2004). Organization of rat vibrissa motor cortex and adjacent areas according to cytoarchitectonics, microstimulation, and intracellular stimulation of identified cells. J. Comp. Neurol. *479*, 360–373.

Brodmann, K., and Gary, L.J. (2006). Brodmann's Localisation in the Cerebral Cortex: The Principles of Comparative Localisation in the Cerebral Cortex Based on Cytoarchitectonics (New York: Springer).

Capra, N.F., and Dessem, D. (1992). Central connections of trigeminal primary afferent neurons: topographical and functional considerations. Crit. Rev. Oral Biol. Med. *4*, 1–52.

Churchland, M.M., Cunningham, J.P., Kaufman, M.T., Foster, J.D., Nuyujukian, P., Ryu, S.I., and Shenoy, K.V. (2012). Neural population dynamics during reaching. Nature *487*, 51–56.

Cunningham, E.T., Jr., and Sawchenko, P.E. (2000). Dorsal medullary pathways subserving oromotor reflexes in the rat: implications for the central neural control of swallowing. J. Comp. Neurol. *417*, 448–466.

Dong, Y., Li, J., Zhang, F., and Li, Y. (2011). Nociceptive afferents to the premotor neurons that send axons simultaneously to the facial and hypoglossal motoneurons by means of axon collaterals. PLoS ONE *6*, e25615.

Donoghue, J.P., and Parham, C. (1983). Afferent connections of the lateral agranular field of the rat motor cortex. J. Comp. Neurol. *217*, 390–404.

Donoghue, J.P., and Wise, S.P. (1982). The motor cortex of the rat: cytoarchitecture and microstimulation mapping. J. Comp. Neurol. *212*, 76–88.

Economo, M.N., Viswanathan, S., Tasic, B., Bas, E., Winnubst, J., Menon, V., Graybuck, L.T., Nguyen, T.N., Smith, K.A., Yao, Z., et al. (2018). Distinct descending motor cortex pathways and their roles in movement. Nature *563*, 79–84.

Erzurumlu, R.S., and Killackey, H.P. (1979). Efferent connections of the brainstem trigeminal complex with the facial nucleus of the rat. J. Comp. Neurol. *188*, 75–86.

Esposito, M.S., Capelli, P., and Arber, S. (2014). Brainstem nucleus MdV mediates skilled forelimb motor tasks. Nature *508*, 351–356.

Fay, R.A., and Norgren, R. (1997a). Identification of rat brainstem multisynaptic connections to the oral motor nuclei in the rat using pseudorabies virus. II. Facial muscle motor systems. Brain Res. Brain Res. Rev. *25*, 276–290.

Fay, R.A., and Norgren, R. (1997b). Identification of rat brainstem multisynaptic connections to the oral motor nuclei using pseudorabies virus. I. Masticatory muscle motor systems. Brain Res. Brain Res. Rev. *25*, 255–275.

Fay, R.A., and Norgren, R. (1997c). Identification of rat brainstem multisynaptic connections to the oral motor nuclei using pseudorabies virus. III. Lingual muscle motor systems. Brain Res. Brain Res. Rev. *25*, 291–311.

Ferezou, I., Haiss, F., Gentet, L.J., Aronoff, R., Weber, B., and Petersen, C.C.H. (2007). Spatiotemporal dynamics of cortical sensorimotor integration in behaving mice. Neuron *56*, 907–923.

Fritsch, G., and Hitzig, E. (2009). Electric excitability of the cerebrum (Uber die elektrische Erregbarkeit des Grosshirns). Epilepsy Behav. *15*, 123–130.

Furuta, T., Nakamura, K., and Deschenes, M. (2006). Angular tuning bias of vibrissa-responsive cells in the paralemniscal pathway. J. Neurosci. *26*, 10548–10557.

Georgopoulos, A.P., Schwartz, A.B., and Kettner, R.E. (1986). Neuronal population coding of movement direction. Science *233*, 1416–1419.

Giannakopoulos, N.N., Hellmann, D., Schmitter, M., Krüger, B., Hauser, T., and Schindler, H.J. (2013). Neuromuscular interaction of jaw and neck muscles during jaw clenching. J. Orofac. Pain *27*, 61–71.

Gonzalez-Joekes, J., and Schreurs, B.G. (2012). Anatomical characterization of a rabbit cerebellar eyeblink premotor pathway using pseudorabies and identification of a local modulatory network in anterior interpositus. J. Neurosci. *32*, 12472–12487.

Graziano, M.S.A. (2016). Ethological action maps: a paradigm shift for the motor cortex. Trends Cogn. Sci. *20*, 121–132.

Graziano, M.S., and Aflalo, T.N. (2007). Mapping behavioral repertoire onto the cortex. Neuron *56*, 239–251.

Graziano, M.S.A., Taylor, C.S.R., and Moore, T. (2002). Complex movements evoked by microstimulation of precentral cortex. Neuron *34*, 841–851.

Grinevich, V., Brecht, M., and Osten, P. (2005). Monosynaptic pathway from rat vibrissa motor cortex to facial motor neurons revealed by lentivirus-based axonal tracing. J. Neurosci. *25*, 8250–8258.

Haiss, F., and Schwarz, C. (2005). Spatial segregation of different modes of movement control in the whisker representation of rat primary motor cortex. J. Neurosci. *25*, 1579–1587.

Harrison, T.C., Ayling, O.G., and Murphy, T.H. (2012). Distinct cortical circuit mechanisms for complex forelimb movement and motor map topography. Neuron *74*, 397–409.

Hattox, A.M., Priest, C.A., and Keller, A. (2002). Functional circuitry involved in the regulation of whisker movements. J. Comp. Neurol. *442*, 266–276.

Hira, R., Terada, S., Kondo, M., and Matsuzaki, M. (2015). Distinct functional modules for discrete and rhythmic forelimb movements in the mouse motor cortex. J. Neurosci. *35*, 13311–13322.

Hiraoka, M., and Shimamura, M. (1977). Neural mechanisms of the corneal blinking reflex in cats. Brain Res. *125*, 265–275.

Hoffer, Z.S., Hoover, J.E., and Alloway, K.D. (2003). Sensorimotor corticocortical projections from rat barrel cortex have an anisotropic organization that facilitates integration of inputs from whiskers in the same row. J. Comp. Neurol. *466*, 525–544.

Hollis, E.R., 2nd, Ishiko, N., Yu, T., Lu, C.C., Haimovich, A., Tolentino, K., Richman, A., Tury, A., Wang, S.H., Pessian, M., et al. (2016). Ryk controls remapping of motor cortex during functional recovery after spinal cord injury. Nat. Neurosci. *19*, 697–705.

Huang, C.S., Hiraba, H., Murray, G.M., and Sessle, B.J. (1989). Topographical distribution and functional properties of cortically induced rhythmical jaw movements in the monkey (Macaca fascicularis). J. Neurophysiol. *61*, 635–650.

Isogai, F., Kato, T., Fujimoto, M., Toi, S., Oka, A., Adachi, T., Maeda, Y., Morimoto, T., Yoshida, A., and Masuda, Y. (2012). Cortical area inducing chewing-like rhythmical jaw movements and its connections with thalamic nuclei in guinea pigs. Neurosci. Res. *74*, 239–247.

Jacquin, M.F., and Rhoades, R.W. (1990). Cell structure and response properties in the trigeminal subnucleus oralis. Somatosens. Mot. Res. *7*, 265–288.

Jacquin, M.F., Woerner, D., Szczepanik, A.M., Riecker, V., Mooney, R.D., and Rhoades, R.W. (1986). Structure-function relationships in rat brainstem subnucleus interpolaris. I. Vibrissa primary afferents. J. Comp. Neurol. *243*, 266–279.

Jeong, M., Kim, Y., Kim, J., Ferrante, D.D., Mitra, P.P., Osten, P., and Kim, D. (2016). Comparative three-dimensional connectome map of motor cortical projections in the mouse brain. Sci. Rep. *6*, 20072.

Kakei, S., Hoffman, D.S., and Strick, P.L. (1999). Muscle and movement representations in the primary motor cortex. Science *285*, 2136–2139.

Kita, T., and Kita, H. (2012). The subthalamic nucleus is one of multiple innervation sites for long-range corticofugal axons: a single-axon tracing study in the rat. J. Neurosci. *32*, 5990–5999.

Kleinfeld, D., Berg, R.W., and O'Connor, S.M. (1999). Anatomical loops and their electrical dynamics in relation to whisking by rat. Somatosensory and Motor Research *16*, 69–88.

Kleinfeld, D., Sachdev, R.N.S., Merchant, L.M., Jarvis, M.R., and Ebner, F.F. (2002). Adaptive filtering of vibrissa input in motor cortex of rat. Neuron *34*, 1021–1034.

Kobayashi, M., Masuda, Y., Fujimoto, Y., Matsuya, T., Yamamura, K., Yamada, Y., Maeda, N., and Morimoto, T. (2002). Electrophysiological analysis of rhythmic jaw movements in the freely moving mouse. Physiol. Behav. *75*, 377–385.

Komiyama, T., Sato, T.R., O'Connor, D.H., Zhang, Y.X., Huber, D., Hooks, B.M., Gabitto, M., and Svoboda, K. (2010). Learning-related fine-scale specificity imaged in motor cortex circuits of behaving mice. Nature *464*, 1182–1186.

Kurnikova, A., Moore, J.D., Liao, S.-M., Deschênes, M., and Kleinfeld, D. (2017). Coordination of orofacial motor actions into exploratory behavior by rat. Curr. Biol. *27*, 688–696.

Kurnikova, A., Deschênes, M., and Kleinfeld, D. (2019). Functional brain stem circuits for control of nose motion. J. Neurophysiol. *121*, 205–217.

Li, Y.-Q., Takada, M., and Mizuno, N. (1993). Premotor neurons projecting simultaneously to two orofacial motor nuclei by sending their branched axons. A study with a fluorescent retrograde double-labeling technique in the rat. Neurosci. Lett. *152*, 29–32.

Li, Y.-Q., Takada, M., Kaneko, T., and Mizuno, N. (1995). Premotor neurons for trigeminal motor nucleus neurons innervating the jaw-closing and jaw-opening muscles: differential distribution in the lower brainstem of the rat. J. Comp. Neurol. *356*, 563–579.

Lim, D.H., Mohajerani, M.H., Ledue, J., Boyd, J., Chen, S., and Murphy, T.H. (2012). In vivo large-scale cortical mapping using channelrhodopsin-2 stimulation in transgenic mice reveals asymmetric and reciprocal relationships between cortical areas. Front. Neural Circuits *6*, 11.

Lin, J.Y., Knutsen, P.M., Muller, A., Kleinfeld, D., and Tsien, R.Y. (2013). ReaChR: A red-shifted variant of channelrhodopsin enables neuronal activation through the intact skull. Nat. Neurosci. *16*, 1499–1508.

Lo, L., and Anderson, D.J. (2011). A Cre-dependent, anterograde transsynaptic viral tracer for mapping output pathways of genetically marked neurons. Neuron *72*, 938–950.

Lund, J.P., Sasamoto, K., Murakami, T., and Olsson, K.A. (1984). Analysis of rhythmical jaw movements produced by electrical stimulation of motor-sensory cortex of rabbits. J. Neurophysiol. *52*, 1014–1029.

Mao, T., Kusefoglu, D., Hooks, B.M., Huber, D., Petreanu, L., and Svoboda, K. (2011). Long-range neuronal circuits underlying the interaction between sensory and motor cortex. Neuron *72*, 111–123.

Matthews, D.W., Deschênes, M., Furuta, T., Moore, J.D., Wang, F., Karten, H.J., and Kleinfeld, D. (2015). Feedback in the brainstem: an excitatory disynaptic pathway for control of whisking. J. Comp. Neurol. *523*, 921–942.

May, P.J., Vidal, P.P., Baker, H., and Baker, R. (2012). Physiological and anatomical evidence for an inhibitory trigemino-oculomotor pathway in the cat. J. Comp. Neurol. *520*, 2218–2240.

McElvain, L.E., Friedman, B., Karten, H.J., Svoboda, K., Wang, F., Deschênes, M., and Kleinfeld, D. (2018). Circuits in the rodent brainstem that control whisking in concert with other orofacial motor actions. Neuroscience *368*, 152–170.

Mimica, B., Dunn, B.A., Tombaz, T., Bojja, V.P., and Whitlock, J.R. (2018). Efficient cortical coding of 3D posture in freely behaving rats. Science *362*, 584–589.

Mitra, P.P., and Bokil, H.S. (2008). Observed Brain Dynamics (New York: Oxford University Press).

Nguyen, Q.-T., and Kleinfeld, D. (2005). Positive feedback in a brainstem tactile sensorimotor loop. Neuron *45*, 447–457.

Olsson, K.A., and Westberg, K.G. (1991). Integration in trigeminal premotor interneurones in the cat. 2. Functional characteristics of neurones in the subnucleus-gamma of the oral nucleus of the spinal trigeminal tract with a projection to the digastric motoneurone subnucleus. Exp. Brain Res. *84*, 115–124.

Oswald, M.J., Tantirigama, M.L., Sonntag, I., Hughes, S.M., and Empson, R.M. (2013). Diversity of layer 5 projection neurons in the mouse motor cortex. Front. Cell. Neurosci. *7*, 174.

Overduin, S.A., d'Avella, A., Carmena, J.M., and Bizzi, E. (2012). Microstimulation activates a handful of muscle synergies. Neuron *76*, 1071–1077.

Paxinos, G., and Franklin, K.B. (2008). The Mouse Brain in Stereotaxic Coordinates (Amsterdam: Academic Press).

Peters, A.J., Chen, S.X., and Komiyama, T. (2014). Emergence of reproducible spatiotemporal activity during motor learning. Nature *510*, 263–267.

Pinganaud, G., Bernat, I., Buisseret, P., and Buisseret-Delmas, C. (1999). Trigeminal projections to hypoglossal and facial motor nuclei in the rat. J. Comp. Neurol. *415*, 91–104.

Reep, R.L., Corwin, J.V., Hashimoto, A., and Watson, R.T. (1987). Efferent connections of the rostral portion of medial agranular cortex in rats. Brain Res. Bull. *19*, 203–221.

Ren, K., and Dubner, R. (2011). The role of trigeminal interpolaris-caudalis transition zone in persistent orofacial pain. Int. Rev. Neurobiol. *97*, 207–225.

Richmond, F.J., Thomson, D.B., and Loeb, G.E. (1992). Electromyographic studies of neck muscles in the intact cat. I. Patterns of recruitment underlying posture and movement during natural behaviors. Exp. Brain Res. *88*, 41–58.

Roucoux, A., Crommelinck, M., and Decostre, M.F. (1989). Neck muscle activity in eye-head coordinated movements. Prog. Brain Res. *80*, 351–362.

Sabino, M.A., Honore, P., Rogers, S.D., Mach, D.B., Luger, N.M., and Mantyh, P.W. (2002). Tooth extraction-induced internalization of the substance P receptor in trigeminal nucleus and spinal cord neurons: imaging the neurochemistry of dental pain. Pain *95*, 175–186.

Sakurai, K., Akiyama, M., Cai, B., Scott, A., Han, B.-X., Takatoh, J., Sigrist, M., Arber, S., and Wang, F. (2013). The organization of submodality-specific touch afferent inputs in the vibrissa column. Cell Rep. *5*, 87–98.

Satoh, Y., Yajima, E., Nagamine, Y., Ishizuka, K., and Murakami, T. (2011). Effects of neck muscle activities during rhythmic jaw movements by stimulation of the medial vestibular nucleus in rats. Brain Res. Bull. *86*, 447–453.

Smith, J.B., Watson, G.D., Alloway, K.D., Schwarz, C., and Chakrabarti, S. (2015). Corticofugal projection patterns of whisker sensorimotor cortex to the sensory trigeminal nuclei. Front. Neural Circuits *9*, 53.

Sreenivasan, V., Karmakar, K., Rijli, F.M., and Petersen, C.C. (2015). Parallel pathways from motor and somatosensory cortex for controlling whisker movements in mice. Eur. J. Neurosci. *41*, 354–367.

Stanek, E., 4th, Cheng, S., Takatoh, J., Han, B.X., and Wang, F. (2014). Monosynaptic premotor circuit tracing reveals neural substrates for oro-motor coordination. eLife *3*, e02511.

Takatoh, J., Nelson, A., Zhou, X., Bolton, M.M., Ehlers, M.D., Arenkiel, B.R., Mooney, R., and Wang, F. (2013). New modules are added to vibrissal premotor circuitry with the emergence of exploratory whisking. Neuron *77*, 346–360.

Taylor, J.E., Wall, J.D., and Welch, D.B. (2017). Masticatory and brux-like motor patterns in the freely behaving rat: electromyography and phase analysis. Trans. Ill. State Acad. Sci. *110*, 1–7.

Tennant, K.A., Adkins, D.L., Donlan, N.A., Asay, A.L., Thomas, N., Kleim, J.A., and Jones, T.A. (2011). The organization of the forelimb representation of the C57BL/6 mouse motor cortex as defined by intracortical microstimulation and cytoarchitecture. Cereb. Cortex *21*, 865–876.

Tsuboi, A., Kolta, A., Chen, C.C., and Lund, J.P. (2003). Neurons of the trigeminal main sensory nucleus participate in the generation of rhythmic motor patterns. Eur. J. Neurosci. *17*, 229–238.

van Ham, J.J., and Yeo, C.H. (1996). Trigeminal inputs to eyeblink motoneurons in the rabbit. Exp. Neurol. *142*, 244–257.

Wang, Q., and Burkhalter, A. (2007). Area map of mouse visual cortex. J. Comp. Neurol. *502*, 339–357.

Wang, H., Peca, J., Matsuzaki, M., Matsuzaki, K., Noguchi, J., Qiu, L., Wang, D., Zhang, F., Boyden, E., Deisseroth, K., et al. (2007). High-speed mapping of synaptic connectivity using photostimulation in channelrhodopsin-2 transgenic mice. Proc. Natl. Acad. Sci. U S A *104*, 8143–8148.

Westberg, K., Clavelou, P., Sandström, G., and Lund, J.P. (1998). Evidence that trigeminal brainstem interneurons form subpopulations to produce different forms of mastication in the rabbit. J. Neurosci. *18*, 6466–6479.

Yoshida, A., Yasuda, K., Dostrovsky, J.O., Bae, Y.C., Takemura, M., Shigenaga, Y., and Sessle, B.J. (1994). Two major types of premotoneurons in the feline trigeminal nucleus oralis as demonstrated by intracellular staining with horseradish peroxidase. J. Comp. Neurol. *347*, 495–514.

STAR★METHODS

KEY RESOURCES TABLE

REAGENT or RESOURCE	SOURCE	IDENTIFIER
Antibodies		
Rabbit anti GFP (made in goat)	Novus	NB600-308, RRID: AB_1048879
Biotinylated anti rabbit IgG (made in goat)	Vector	BA-1000, RRID: AB_2336201
Goat anti rabbit conjugated with Alexa 488	Invitrogen	A-11034, RRID: AB_221544
DAB tetrahydrochloride	Sigma	D5637-5G
Cytochrome C	Sigma	C-2506
Bacterial and viral strains		
Pseudorabies-GFP (strain 152)	Enquist lab	N/A
Lentivirus-CAG-synaptophysin-eGFP	Adrian Lozada	N/A
Retrograde lentivirus-hsyn-Cit	Daniel Gibbs	N/A
AAV2.5-hsyn-flex-Cit	John Lin (Lin et al., 2013)	N/A
AAV2.5-hsyn-flex-ReaChR-Cit	Salk Virus Core	Special preparation
AAV retro-hsyn-Cre	UPenn Virus Core	Special preparation
AAV-DJ-hsyn-flex-mGFP-2a-mRuby	Stanford Virus Core	GVVC-AAV-100
Retrograde lentivirus-hsyn-Cre	Fan Wang	N/A
Deposited data		
Raw data	This paper	N/A
Experimental models: Organisms/strains		
Mouse: C57BL/6J	Jackson Laboratories	#000664, RRID: MGI:5657312
Thy1-ChR2-YFP alias B6.Cg-Tg(Thy1-COP4/EYFP) 18Gfng/J	Jackson Laboratories (Arenkiel et al., 2007; Wang et al., 2007)	#007612, RRID: IMSR_JAX:007615
Software and algorithms		
MATLAB	Mathworks	2007b to 2017b
Chronux	Chronux.org	http://chronux.org
FIJI	NIH	http://imagej.net/Fiji

LEAD CONTACT AND MATERIALS AVAILABILITY

Further information and requests for resources and reagents should be directed and will be fulfilled by the Lead Contact, David Kleinfeld (dk@physics.ucsd.edu). This study did not generate new unique reagents.

EXPERIMENTAL MODEL AND SUBJECT DETAILS

Mice

50 female C57BL/6 mice and 5 female Thy1-ChR2 mice (JAX strain B6.Cg-Tg (Thy1-COP4/EYFP)18Gfn/J) (Arenkiel et al., 2007) age 5 - 18 weeks contributed to this study. All experimental procedures followed the Guide for the Care and Use of Laboratory Animals and has been approved by the Institutional Animal Care and Use Committee at the University of California, San Diego.

METHOD DETAILS

Muscle Injections

Nine C57BL/6 mice were anesthetized in a box with 2% (v/v) isoflurane with oxygen until they did not respond to a toe pinch. A single injection of 500 nL of pseudorabies was injected into either the whisker pad, the anterior belly of the digastric muscle, or the biceps brachii muscle. 75 to 80 h later the mice were deeply anesthetized with pentobarbitol before being transcardially perfused with a 0.01 mM phosphate buffered salt solution (PBS) followed by 4% (w/v) paraformaldehyde in PBS.

Brain Injections

Each animal was anesthetized with 2% (v/v) isoflurane with oxygen until they did not respond to a toe pinch. Body temperature was maintained at 37°C (no. 40-90-8; FHC Inc.) and isoflurane decreased to 1.5% (v/v) once placed in the stereotaxic frame (Kopf). The fur above the skull was cleaned with betadine before being cut to open access to the skull. Small holes were drilled over the motor cortex and/or the spinal trigeminal nucleus (EXL-M40, Osada, CA, USA). Injections were made using a Nanojet (Drummond). Anterior-posterior (AP) and medial-lateral (ML) coordinates are relative to Bregma, while dorsal-ventral coordinates are relative to the surface of the brain, as follows: jaw motor cortex = AP +3 mm, ML 2 mm, DV 0.8 mm; dorsal SpVO = AP –5.4 mm, ML 2.0 mm lateral, DV 3.9 - 4.1 mm; SpVIr = AP –5.7 mm, ML 2.0 mm, DV 4.2-4.5 mm; facial nucleus = AP –5.0 mm, ML 1.5 mm, DV 6.0 mm. Coordinates for SpVO and SpVIr were confirmed by electrophysiology recordings probing somatosensory responses prior to injecting. Coordinates for the facial nucleus were determined from intercranial microstimulation. For virus details, see Table S1.

Headbar Placement

Six C57BL/6 mice and nine Thy1-ChR2 mice were anesthetized and placed in a stereotaxic apparatus as described above. The fur over the skin was cleaned with betadine before a straight anterior posterior cut was opened from the nasal to the intraparietal bone. A 4 mm diameter cranial window was made over the frontal bone with a centroid over the spot AP +2 mm, ML 2 mm. A thin layer of ACSF was applied before a 4 mm diameter glass coverslip (Fisher Brand) was gently placed over the brain surface. A small amount of cyanoacrylate glue was used to seal the bone to the glass. Once the glue was dry, the remaining exposed skull was cleaned and layered with cyanoacrylate glue. Once dry, a metal headbar was attached to the skull via cyanoacrylate glue. Last, a layer of dental cement covered the headbar and skull.

Optogenetic Stimulation Experiments

The scan maps and specific positions of the laser were made using a scan system of Murphy and colleagues (Lim et al., 2012) (Figure 1A). Either a blue 446 nm laser (Cube; Coherent Inc.) or a red 637 nm laser (Obis; Coherent Inc.) was scanned. The scan objective, effective NA of 0.01, was used to create a focal spot of 35 μm in diameter

Electrodes for EMGs were made of 50 μm diameter insulated tungsten wire (AM systems 795500). The tip of the wire for recording was stripped 1 mm before threaded through a 30-gauge needle and hooked. EMGs were inserted at the beginning of each recording session while the mice were under light (0.5–1.0%) isoflurane. Two EMGs electrodes were inserted in each muscle, i.e., biceps brachii, digastric, intrinsic vibrissa, masseter, quadriceps, or splenius capitis. Three to five muscles were recorded per session. EMG recordings were taken using individual amplifiers for each muscle (DAM 80, World Precision Instruments) at 10 kHz. The raw signals were processed for extraction of the EMG envelope by using an 8^{th} order Butterworth filter between 250 Hz and 2.5 kHz in the forward and reverse direction, then rectified by taking the absolute value, followed by a low pass 2^{nd}-order Butterworth filter at 50 Hz in the forward and reverse directions. Last, a median filter was applied.

Videography were used to track the forelimb, jaw, nose, and vibrissae. Nose and vibrissa videographs were taken from above. The forelimb and jaw utilized two mirrors, one in front and one to the side, that reflected the front image of the mouse up to the camera above. A high speed, 1000 by 1000-pixel camera was used with a frame rate of 200 frames per second (no. A504K; Basler Vision Technologies). For vibrissa tracking, one vibrissa was painted (Tulip dimensional fabric paint, 65101) for light contrast imaging with a mask for live tracking. For nose and jaw tracking, a dot of paint was placed on the top of the nose or the center bottom of the jaw. Forelimb tracking focused bright light on the paws.

Histology

After perfusion, brains were left in 4% (w/v) paraformaldehyde in PBS between 4 and 24 h and then cryoprotected in 30% (w/v) sucrose in PBS. Sections were collected on a sliding microtome maintained between −21 and −24°C. For synapse reconstructions, sections were cut horizontally at 16 μm and mounted on slides prior to immunostaining. For cell reconstructions, sections were cut at 60 μm and every other section was immunostained free floating. The synapse and cell labeling was converted to dark product using rabbit anti GFP (Novus; 1:1000 (v/v) in a 2% (v/v) goat block solution in PBS), biotinylated anti-rabbit secondary antibodies (1:200 (v/v) in goat block), amplified with ABC kit (Vector Labs) and converted to dark product with the SG kit (Vector Labs). Slides were processed with increasing ethanol concentrations, followed by xylines, before being coverslipped with DPX (Sigma). All slides with dark product were counterstained with cytochrome oxidase. Slides or free-floating sections were incubated in cytochrome oxidase (37.5 mL PBS + 1.5 g sucrose + 33 mg DAB tetrahydrochloride (Sigma D5637-5G) + 15 mg cytochrome C (Sigma C-2506)) and maintained at 37°C for 1 - 3 h. All slides were scanned on a Hammamatsu Nanozoomer and loaded into Neurolucida and then MATLAB for three-dimensional reconstruction. Fluorescent sections were cut between 30 and 50 μm. Citrine containing sections were amplified with rabbit anti GFP (Novus; 1:1000 in goat block) and Alexa 488 conjugated goat anti rabbit (Invitrogen; 1:1000 (v/v) in goat block) and coverslipped with Fluoromount (Southern Biotech). 16-bit images were collected on a fluorescent microscope and analyzed in ImageJ.

Computational Analyses

All code was written in MATLAB (The Mathworks). For the spectral analysis we used the Chronux package (Mitra and Bokil, 2008). Composite maps in Figure 2F were created by taking the average amplitude within the trial, then averaging all trials at a given location

across all animals (20 trials in each of five mice) and interpolating linearly between locations. Clusters identified in Figure 4E were found using a 2-D density plot of data in Figure 4D.

QUANTIFICATION AND STATISTICAL ANALYSIS

Statistical Tests

Statistical tests are identified in the Results section. To identify if EMG signals were significantly different from baseline in Figure 1 we used a K-S test with $p < 0.001$. To compare normalized muscle activation across muscles in Figure 7 we used an ANOVA test with $p > 0.1$. To compare activation of muscle EMG from baseline in Figure 7 we used a Student's t test with $p < 0.05$. In Figures 7F, 7G, 7I, and 7J, greyed out traces and graph markers indicate that the result was not significant. All activation analysis used all data taken during the stimulus period and compared it with an equal period of time during the baseline period.

Quantification

All quantification of synapses and neurons in Neurolucida or FIJI. For 3-D reconstructions in Figures 4, 5, and S5, Neurolucida was used to both count and identify coordinate location of each synapse or neuron. To create sagittal projections and histograms in Figures 5 and S5, Neurolucida data were exported to MATLAB. For density quantification in Figure 4E, neurons were counted within the peak density region of the 2-D histogram as described in the figure legend. For density quantification for Figures 4J and 6C, 5–8 sections were taken at even intervals through a structure. An area outline was created around the structure in FIJI based on histological markers except for motor cortex in which the outline was create around the injection site as marked by the presence of neurons and their prominent dendrites (white outlines in Figures 4, 6, and S6). All presynaptic terminals were identified by co-labeling of mRuby and GFP within the white outlines. Volume of a structure in one image was calculated by multiplying the area of the structure, as identified by the white outline, by the thickness of the section. For each section, the number of synapses were divided by the volume and final density was calculated by averaging across sections (Table S2).

DATA AND CODE AVAILABILITY

The datasets generated during this study are available in Table S2.